HAL
open science

Crystal structures, frustrated magnetism, and chemical pressure in Sr-doped Ba_3 Ni Sb_2 O_9 perovskites

Mélanie Viaud, Catherine Guillot-Deudon, Eric Gautron, Maria Teresa Caldes, Guido Berlanda, Philippe Deniard, Philippe Boullay, Florence Porcher, Carole La, C. Darie, et al.

To cite this version:

Mélanie Viaud, Catherine Guillot-Deudon, Eric Gautron, Maria Teresa Caldes, Guido Berlanda, et al.. Crystal structures, frustrated magnetism, and chemical pressure in Sr-doped Ba_3 Ni Sb_2 O_9 perovskites. Physical Review Materials, 2022, 6 (12), pp.124408. 10.1103/PhysRevMaterials.6.124408 . hal-03963204

HAL Id: hal-03963204

https://hal.science/hal-03963204v1

Submitted on 30 Jan 2023

HAL is a multi-disciplinary open access archive for the deposit and dissemination of scientific research documents, whether they are published or not. The documents may come from teaching and research institutions in France or abroad, or from public or private research centers.

L'archive ouverte pluridisciplinaire **HAL**, est destinée au dépôt et à la diffusion de documents scientifiques de niveau recherche, publiés ou non, émanant des établissements d'enseignement et de recherche français ou étrangers, des laboratoires publics ou privés.

Crystal structures, frustrated magnetism, and chemical pressure in Sr-doped $Ba_3NiSb_2O_9$ perovskites

Mélanie Viaud,[1] Catherine Guillot-Deudon,[1] Eric Gautron,[1] Maria Teresa Caldes,[1] Guido Berlanda,[2] Philippe Deniard,[1] Philippe Boullay,[3] Florence Porcher,[4] Carole La,[5] Céline Darie,[6] A. Zorko,[7,8] A. Ozarowski,[9] Fabrice Bert,[2] Philippe Mendels,[2,*] and Christophe Payen[1,†]

[1]*Nantes Université, CNRS, Institut des Matériaux de Nantes Jean Rouxel, IMN, F-44000 Nantes, France*
[2]*Laboratoire de Physique des Solides, Université Paris-Saclay, CNRS, 91405 Orsay, France*
[3]*CRISMAT laboratory, UMR6508, Normandie University, ENSICAEN, UNICAEN, CNRS, Caen 14050 France*
[4]*Laboratoire Léon Brillouin, CEA Saclay, CNRS UMR12, F-91191 Gif-sur-Yvette, France*
[5]*Nantes Université, CNRS, UMR 6112, Laboratoire de Planétologie et Géosciences, F-44000 Nantes, France*
[6]*Université Grenoble Alpes, CNRS, Grenoble INP, Institut Néel, 38000 Grenoble, France*
[7]*Jožef Stefan Institute, Jamova c. 39, 1000 Ljubljana, Slovenia*
[8]*Faculty of Mathematics and Physics, University of Ljubljana, Jadranska u. 19, 1000 Ljubljana, Slovenia*
[9]*National High Magnetic Field Laboratory, Florida State University, Tallahassee, Florida 32310, USA*

(Received 3 June 2022; accepted 16 November 2022; published 20 December 2022)

The effects of chemical pressure on the structural and magnetic properties of the triple perovskite $Ba_3NiSb_2O_9$ are investigated by substituting Sr^{2+} ions for Ba^{2+} ions. Two $Ba_{3-x}Sr_xNiSb_2O_9$ phases could be stabilized via a solid-state reaction at ambient pressure (AP) in air. The 6*H* with Sb_2O_9 pairs ($x = 0$) → 6*H* with $NiSbO_9$ pairs ($x = 0.5$) → 3*C* (cubic with corner-sharing octahedral, $x = 1.25$) sequence of structural phases occurs with increasing Sr content, i.e., chemical pressure, which is like that previously reported for pure samples of $Ba_3NiSb_2O_9$ obtained under increasing high physical pressure (HP). For the 6*H* $Ba_{2.5}Sr_{0.5}NiSb_2O_9$ ($x = 0.5$) phase, using combined Rietveld refinements of powder x-ray and neutron diffraction patterns, precession electron diffraction tomography data collected on thin crystals, aberration-corrected high-angle annular dark field scanning transmission electron microscopy coupled to energy dispersive x-ray spectroscopy mapping, we reach the conclusion that the structure features corner-sharing SbO_6 octahedra and $NiSbO_9$ pairs of face-shared octahedra (or Ni-Sb dumbbells) with either a random orientation of the Ni-Sb dumbbells or nanosized chemical correlations for the dumbbell arrangement. As observed in HP $Ba_3NiSb_2O_9$ produced through synthesis at 9 GPa, AP $Ba_{1.75}Sr_{1.25}NiSb_2O_9$ ($x = 1.25$) crystallizes in a 3*C* double perovskite $A_2BB'O_6$ cubic structure where *A*, *B*, and *B*′ sites are occupied by (Ba + Sr), Sb, and ($\frac{2}{3}$Ni + $\frac{1}{3}$Sb) atoms, respectively. The *B*′ sites, which are randomly occupied by spin-1 Ni^{2+} and diamagnetic Sb^{5+}, form a face-centered-cubic (FCC) sublattice where the Ni^{2+} amount stays above the site percolation threshold. Weiss temperatures (≈ -65 and ≈ -213 K for $Ba_{2.5}Sr_{0.5}NiSb_2O_9$ and $Ba_{1.75}Sr_{1.25}NiSb_2O_9$, respectively) indicate that dominant magnetic interactions between Ni^{2+} spins are antiferromagnetic with magnitudes like those observed in the corresponding HP phases of pure $Ba_3NiSb_2O_9$. As for the 6*H* HP $Ba_3NiSb_2O_9$ compound, in 6*H* $Ba_{2.5}Sr_{0.5}NiSb_2O_9$, muon spin relaxation ($\mu$SR) measurements identify a dynamic magnetic state down to the base temperature (95 mK), consistent with a previously published inelastic neutron scattering study. For 3*C* $Ba_{1.75}Sr_{1.25}NiSb_2O_9$, μSR and ^{121}Sb nuclear magnetic resonance measurements both indicate the presence of a transition to a static magnetic state below 11(1) K with a significant amount of disorder in this frozen state, in contrast to the spin-liquid state previously suggested for the 3*C* HP phase of $Ba_3NiSb_2O_9$. Consistently, a broad maximum is observed in the specific heat at the same temperature. Building on the structural data, the magnetic properties of HP 6*H* $Ba_3NiSb_2O_9$ and AP 6*H* $Ba_{2.5}Sr_{0.5}NiSb_2O_9$ are discussed in light of recent works on triangular and J_1-J_2 honeycomb systems with or without quenched disorder. We are led to the conclusion that the driving force toward a spin-liquid-like state is quenched disorder which needs to be incorporated in J_1-J_2 honeycomb models. Our evidence of a magnetic transition to a frozen magnetic ground state for the AP Sr-doped 3*C* phase is in line with models for geometrically frustrated FCC antiferromagnets. This calls for a better experimental and possibly theoretical understanding of the HP 3*C* phase.

DOI: 10.1103/PhysRevMaterials.6.124408

*philippe.mendels@universite-paris-saclay.fr
†christophe.payen@cnrs-imn.fr

 ©2022 American Physical Society

I. INTRODUCTION

Over the last decades, the study of frustrated spin models and frustrated magnetic materials has opened avenues in the field of magnetism. It has indeed produced a wealth of magnetic phases whose stabilization depends on the nature of frustration originating from the crystal structure. This spans a wide variety from exotic quantum spin liquids (QSLs) or valence bond solid (VBS) phases to finely frustration-tuned long-range ordered states where quantum fluctuations survive. They can be stabilized on a variety of two-dimensional or three-dimensional (3D) spin lattices, e.g., triangular, kagome, J_1-J_2 honeycomb, pyrochlore, face-centered-cubic (FCC), which can be realized in some transition metal or rare earth solid-state compounds. However, identifying the spin Hamiltonian parameters and the associated various energy scales for real systems proves in many cases to be difficult even when average crystal structures are known accurately. In a context where frustration generates many possible and close-by in energy competing states, this constitutes a bottleneck in comparison with ideal models still under study.

Within the past few years, the realm of materials has also led to consideration of the impact of disorder on ground state selection. For instance, the recently discovered triangular-lattice-based material $YbMgGaO_4$ [1–3], which harbors an unexpected spin-liquid-like ground state, has been the subject of significant discussions. The main issues are the determination of its exchange parameters and the role of intrinsic structural disorder associated with the random occupation of the same crystallographic position by nonmagnetic Mg^{2+} and Ga^{3+} ions [4,5]. This in turn triggered conceptual approaches encompassing disorder [6] which might shed light on the physics of numerous frustrated materials.

The family of triple-perovskite materials $Ba_3MSb_2O_9$ (M = Co, Ni, Cu) has recently received a good deal of attention since some of these insulating oxides were identified as realizations of triangular lattice antiferromagnets or as candidates for QSL states [7–12]. These materials exhibit an even richer variety of structural and magnetic properties. The 6H perovskite $Ba_3CoSb_2O_9$, for instance, comprises a long-sought triangular lattice of $S_{\text{eff}} = \frac{1}{2}$ Co^{2+} which exhibits a field-induced up-up-down phase and quantum fluctuation effects in its magnon spectrum [13–15]. The $S = \frac{1}{2}$ Cu^{2+} compound shows considerable deviation from this archetypal triangular antiferromagnetic lattice because of differences in crystal structures. Indeed, in the 6H structure of $Ba_3CuSb_2O_9$, B sites of the B_2O_9 face-sharing bi-octahedra are occupied by Sb^{5+} and Cu^{2+} ions, leading to the formation of asymmetric Cu-Sb dumbbells exclusively (instead of Sb-Sb dumbbells as for 6H $Ba_3CoSb_2O_9$) [10]. An experimental and theoretical consensus has emerged from numerous studies showing that, at the local structural level, these dumbbells arrange in a very short-range honeycomb lattice with strong disorder [10,16–19]. The resulting state does not show any magnetic ordering but displays strong orbital correlations, and its ground state is referred to as a quantum spin-orbital entangled liquid [20].

As for the Ni^{2+} ($S = 1$) nickel-based perovskites, which are the focus of this paper, a QSL state was suggested in the so-called 6HB high-pressure (HP) phase of $Ba_3NiSb_2O_9$ [12]. This 6HB compound is prepared in polycrystalline form by treating the so-called 6HA ambient pressure (AP) polytype of $Ba_3NiSb_2O_9$ under a pressure of a few gigapascals [12,21]. The HP 6HB form differs from the AP 6HA phase in that its crystal structure consists of a $NiSbO_9$ pair of face-sharing octahedra, or Ni-Sb dumbbell (instead of Sb_2O_9 bi-octahedra as for the 6HA form), connected by their vertices to single corner-sharing SbO_6 octahedra (instead of NiO_6 octahedra as for the 6HA phase) [12,21,22]. In the $P6_3mc$ hexagonal crystal structure of 6HB $Ba_3NiSb_2O_9$ as described by Cheng *et al.* [12] based on x-ray diffraction data, the Ni-Sb dumbbells all have the same vertical orientation (all-up arrangement) so that the Ni^{2+} ions form a spin-1—less studied than $S = \frac{1}{2}$—triangular lattice within each triangular layer of $NiSbO_9$ bi-octahedra [Fig. 1(a)]. The magnetic triangular lattices are stacked along the hexagonal c axis and are separated from each other by two nonmagnetic layers of SbO_6 octahedra. A more recent structural investigation of independently prepared samples of HP 6HB $Ba_3NiSb_2O_9$ revealed a different crystal structure [23]. Combined Rietveld refinements of powder x-ray and neutron diffraction patterns were obtained with the

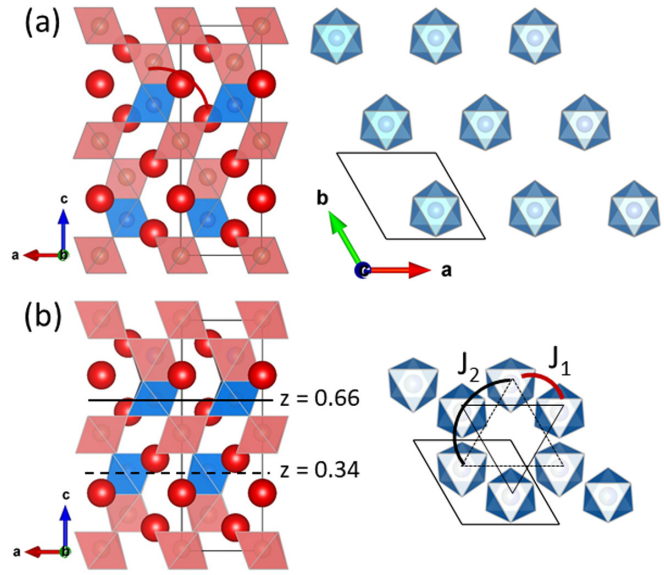

FIG. 1. Reported room-temperature crystal structures of the so-called 6HB high-pressure form of $Ba_3NiSb_2O_9$. These structures contain $NiSbO_9$ pairs of face-sharing octahedra (Ni-Sb dumbbells), connected by their vertices to single SbO_6 octahedra. SbO_6 and NiO_6 octahedra are shaded pink and blue, respectively. Red spheres represent Ba^{2+} ions. Thin solid lines depict unit cells. (a) $P6_3mc$ hexagonal structure [$a = 5.7925(2)$ Å; $c = 14.2918(6)$ Å] with all-up arrangement of Ni-Sb dumbbells [12], viewed along the b axis. Ni^{2+} ions form AB-stacked triangular lattices in the ab plane (right). (b) One of the two possible domains with trigonal symmetry, space group $P3$, and down-up stacking of Ni-Sb dumbbells along the c axis [23]. The other type of domain (not shown) has a reversed up-down stacking of Ni-Sb dumbbells, so that the average structure over many domains is described in the centrosymmetric space group $P6_3/mmc$ [$a = 5.7926(2)$ Å; $c = 14.2841(6)$ Å]. In each domain, two adjacent Ni layers (visualized with horizontal lines at $z = 0.34$ and 0.66), which are separated from each other by only one layer of nonmagnetic Sb, forms a J_1-J_2 honeycomb bilayer (right) [24]. J_1 and J_2 are the interplane and in-plane couplings, respectively.

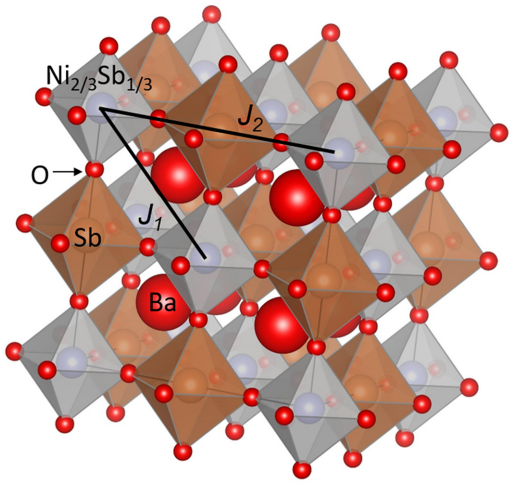

FIG. 2. Room-temperature $Fm\bar{3}m$ structure adopted by 3C phase of $Ba_3NiSb_2O_9$ produced at 9 GPa [12]. This phase has a $Ba_2BB'O_6$ double cubic perovskite structure with the BO_6 octahedra occupied by Sb and the B' octahedral sites in a random manner by ($\frac{2}{3}$Ni + $\frac{1}{3}$Sb) atoms. The B' octahedral sites form an undistorted face-centered-cubic (FCC) sublattice. J_1 and J_2 are the nearest neighbor and next-nearest neighbor interaction between Ni^{2+} ions.

distinct hexagonal centrosymmetric space group $P6_3/mmc$. Furthermore, precession electron diffraction on thin crystals indicated that the actual symmetry is at most trigonal. Nonetheless, the HP phase was still termed 6HB in subsequent works on its magnetic properties. To reconcile differences between powder diffraction and electron diffraction results, it was suggested that crystallites contain domains of small dimensions (1–10 nm) in which the orientations of the Ni-Sb dumbbells alternate between adjacent $(NiSbO_9)_\infty$ bilayers; in each domain, an up-down or down-up stacking is observed along the c axis, as shown in Fig. 1(b). The Ni triangular layers are therefore separated from each other alternately by one and three layers of nonmagnetic SbO_6 octahedra (instead of two for the $P6_3mc$ structure in Ref. [12]). Because the two adjacent Ni ions that are separated by only one nonmagnetic SbO_6 layer along the c axis are likely to interact via Ni-O-O-Ni superexchange, Quilliam *et al.* [24] suggested that the structure contains magnetic bilayers described by a J_1-J_2 buckled honeycomb model at the local level [Fig. 1(b)]. The bulk magnetic susceptibility was very similar to that reported earlier [12], showing a Weiss temperature of −76 K [24]. Muon spin rotation (μSR) and ^{121}Sb nuclear magnetic resonance (NMR) measurements showed that it exhibits a gapless QSL-like ground state [24]. No static magnetism was indeed observed down to temperature as low as 20 mK. NMR results further suggested some structural disorder of unknown origin. Upon applying pressure up to 9 GPa, 6HA $Ba_3NiSb_2O_9$ transforms into a cubic 3C phase with total elimination of face-sharing octahedra [12], as observed in HP $Ba_3ZnSb_2O_9$ [21]. This 3C phase can be described as a $Ba_2BB'O_6$ double cubic perovskite where BO_6 and $B'O_6$ corner-sharing octahedra are occupied by Sb and ($\frac{2}{3}$Ni + $\frac{1}{3}$Sb) atoms, respectively (Fig. 2) [12]. The B' sites form a FCC sublattice. This 3C HP phase of $Ba_3NiSb_2O_9$ was also identified as candidate spin-liquid compounds with a Weiss temperature of −180 K [12].

In this paper, we explore a different route to obtain 6H and 3C phases by replacing Ba^{2+} with Sr^{2+} in $Ba_3NiSb_2O_9$. The Sr^{2+} ion, which is smaller in size than Ba^{2+} (ionic radii 1.44 vs 1.61 Å in 12-coordinate [25]), can be used as a chemical substituent for generating chemical pressure and thus for tuning the structural and magnetic properties of Ba-containing perovskites [26–28]. Here, our goal is to prepare and characterize thermodynamically stable phases that may host quantum paramagnetic states including QSL. Polycrystalline samples of $Ba_{3-x}Sr_xNiSb_2O_9$ with nominal $x \leqslant 1.25$ have been prepared at AP conditions. The structural and magnetic properties of two single-phased Sr-substituted samples, namely, 6H $Ba_{2.5}Sr_{0.5}NiSb_2O_9$ ($x = 0.5$) and 3C $Ba_{1.75}Sr_{1.25}NiSb_2O_9$ ($x = 1.25$), have been studied using diffraction techniques, electron microscopy, bulk susceptibility, ^{121}Sb NMR, and μSR experiments to identify unambiguously their magnetic ground states. Results obtained for these two AP Sr-substituted compounds have been compared with published works related to the corresponding HP phases of pure $Ba_3NiSb_2O_9$. A previously published inelastic neutron scattering (INS) study of a polycrystalline sample of 6H $Ba_{2.5}Sr_{0.5}NiSb_2O_9$ obtained via the same AP synthesis method evidenced the absence of long-range magnetic order down to 0.05 K and suggested that the magnetic excitation spectrum is characteristic of a spin liquid [29]. Our paper ends with a discussion of these results in the framework of existing models with respect to the possible schemes of magnetic interactions, which for both 6H and 3C phases, should certainly encompass a strong disorder component.

II. EXPERIMENTAL METHODS

Two independent series of powder samples of $Ba_{3-x}Sr_xNiSb_2O_9$ with targeted compositions $x = 0$, 0.1, 0.25, 0.5, 0.75, 1, and 1.25 were prepared by using a conventional solid-state reaction route at AP [30]. Samples were furnace cooled at the end of the final heat treatment to avoid quenching high-temperature disordered structural arrangements. The samples were characterized using several techniques, including laboratory powder x-ray diffraction (XRD), scanning electron microscopy (SEM), energy dispersive x-ray spectroscopy (EDS), inductive coupled plasma (ICP) analysis, and volumetric mass density measurements [30]. For both series, single-phased samples were obtained for $x = 0$, 0.1, 0.5, and 1.25, whereas mixtures of two different crystallized phases were observed for other nominal compositions. Initial analyses of XRD patterns suggested that the two single-phased $x = 0$ and 0.1 samples crystallize with the $P6_3/mmc$ crystal symmetry expected for the AP 6HA phase of $Ba_3NiSb_2O_9$ [22]. These initial analyses also suggested that the $x = 0.5$ and 1.25 samples crystallize with the crystal symmetries initially reported for the 6HB (space group $P6_3mc$) and 3C (space group $Fm\bar{3}m$) HP phases of $Ba_3NiSb_2O_9$, respectively [12]. Judging from XRD, the 6HA → 6HB → 3C sequence of structural phases can therefore be stabilized in the case of chemical pressure, like for physical pressure. The refined lattice parameters of the $x = 0.5$ and 1.25 samples were found to be slightly

smaller than those observed for the 6HB and 3*C* phases of HP $Ba_3NiSb_2O_9$ produced during syntheses at 3 and 9 GPa, respectively [30]. This finding suggests that the substitution-induced chemical pressures are a bit higher than the relaxed external pressure in the corresponding HP samples.

Neutron powder diffraction (NPD) data were collected at 300 K on $Ba_{2.5}Sr_{0.5}NiSb_2O_9$ ($x = 0.5$) and $Ba_{1.75}Sr_{1.25}NiSb_2O_9$ ($x = 1.25$) powder samples using the 3T2 instrument (incoming wavelength of $\lambda \approx 1.2247$ Å) at Laboratoire Léon Brillouin (CEA Saclay-CNRS). Rietveld analyses of the XRD and NPD data were performed using JANA2006 [31]. Crystal structures were drawn using VESTA software [32]. As the scattering lengths of Ba, Sr, Ni, Sb, and O depend on the diffraction technique employed (x-ray or neutron), combined Rietveld refinements of XRD and NPD patterns were performed to provide more meaningful descriptions of the average structures of the samples. Neutrons scattering lengths b are 5.07, 7.02, 10.3, 5.57, and 5.803 fm for Ba($Z = 56$), Sr($Z = 38$), Ni($Z = 28$), Sb($Z = 51$), and O($Z = 8$) atoms, respectively. The Ni-Sb contrasts obtained with x rays and neutrons are opposite: $Z(\mathrm{Ni})/Z(\mathrm{Sb}) = 0.549$ and $b_{\mathrm{Ni}}/b_{\mathrm{Sb}} = 1.849$. As the neutron wavelength is known with less accuracy than that of x rays, its value was also refined during the procedure. Cell metrics were therefore determined from XRD patterns [30]. The large samples used for the NPD contained a trace amount of $Ba_3SrSb_2O_9$ impurity phase.

Precession electron diffraction tomography (PEDT) was performed with a Jeol 2010 electron microscope (operating at 200 kV with a LaB6 cathode) equipped with a Nanomegas DigiStar precession module and an upper-mounted Gatan ORIUS 200D CCD camera. PEDT datasets of nonoriented patterns were recorded on several different thin crystals of $Ba_{2.5}Sr_{0.5}NiSb_2O_9$. For data collections, the precession angle was set to 1.4° with a goniometer tilt step 1°. PEDT datasets were analyzed using the computer programs PETS [33] and JANA2006 [31].

High-angle annular dark field scanning transmission electron microscopy (HAADF-STEM) was performed on the sample $Ba_{2.5}Sr_{0.5}NiSb_2O_9$ ($x = 0.5$) with a Themis Z G3 (Thermo Fisher Scientific) operated at 300 kV. This microscope is equipped with a Cs probe corrector (point resolution better than 60 pm) and a Super-X system (4 EDX detectors) allowing us to acquire elemental maps with atomic resolution. The powder was dispersed in ethanol (10 min in ultrasonic bath). A drop of this solution was deposited on a copper grid covered with a thin holey carbon film.

Commercial superconducting quantum interference device magnetometers (Quantum Design, MPMS) were used to collect dc magnetization data. Heat capacity measurements were performed in a multipurpose device (Quantum Design, PPMS), using a semi-adiabatic relaxation technique coupled with a 2τ analysis. To evaluate the lattice contribution in 3*C* $Ba_{1.75}Sr_{1.25}NiSb_2O_9$, the nonmagnetic isostructural compound 3*C* $Ba_{1.75}Sr_{1.25}ZnSb_2O_9$ was also investigated. This latter compound was synthesized in ceramic form by a solid-state reaction route like that used for preparing 3*C* $Ba_{1.75}Sr_{1.25}NiSb_2O_9$.

μSR measurements were performed on the GPS and LTF instruments at the Paul Scherrer Institut and on the EMU spectrometer at the ISIS muon facility, in zero field (ZF) and longitudinal applied field geometries, down to 20 mK for 6*H* $Ba_{2.5}Sr_{0.5}NiSb_2O_9$ and 3*C* $Ba_{1.75}Sr_{1.25}NiSb_2O_9$. ^{121}Sb NMR experiments were performed for the 3*C* $Ba_{1.75}Sr_{1.25}NiSb_2O_9$ phase only, in the 1.2–60 K T range, by sweeping the magnetic field in the $H = 5$–7 T range at a 61.148 MHz fixed frequency and using a standard spin-echo technique.

III. RESULTS

A. Crystal structures

1. 6H $Ba_{2.5}Sr_{0.5}NiSb_2O_9$ ($x = 0.5$)

The published $P6_3mc$ or $P6_3/mmc$ crystal structures of 6HB $Ba_3NiSb_2O_9$ produced during HP experiments [12,23] were used as starting models for combined refinements of our XRD and NPD data. Positions of the Bragg reflections are the same for both models. We first performed attempts with the noncentrosymmetric $P6_3mc$ model that was used for refining a powder XRD pattern of HP 6HB $Ba_3NiSb_2O_9$ [12]. Within this model, the $NiSbO_9$ pairs all have the same orientation [Fig. 1(a)]. This $P6_3mc$ model failed to reproduce the observed intensities. Clear discrepancy between observed and calculated structure factors was obtained for several reflections. This result prompted us to test the alternating centrosymmetric $P6_3/mmc$ model with only one crystallographic Wyckoff $4f$ position and mixed Ni/Sb occupancy for the two octahedral sites of a face-sharing bi-octahedra. A mirror plane at $z = \frac{1}{4}$, which is absent in space group $P6_3mc$, passes through the common triangular face of the bi-octahedra. This causes a difference in structure factors and thus in reflection intensities between $P6_3mc$ and $P6_3/mmc$ models. For our powder sample of $Ba_{2.5}Sr_{0.5}NiSb_2O_9$, the $P6_3/mmc$ model led to a satisfactory level of agreement between observed and calculated patterns. Figure 3 presents the final Rietveld plots. Table I shows the refined structural parameters and final agreement factors. Selected bond distances are listed in Table II. Maximum and minimum electron densities in the difference Fourier map were 0.88 and −1.1 electron A^3, respectively. Atomic coordinates and atomic displacement parameters (ADP) were kept identical for Ba1 and Sr1, for Ba2 and Sr2, and for Sb1 and Ni1 atoms. Anisotropic ADP for Ba/Sr sites and isotropic ADP for the other sites were refined with full occupancies of all sites. Sr is located at both $2b$ and $4f$ Ba positions. There was no detectable Sb2/Ni1 site mixing. The two central sites of the pair of face-shared octahedra (Wykoff $4f$ positions) are almost equally occupied by Ni and Sb atoms. The Ni-Sb distance of 2.66 Å in the $NiSbO_9$ unit is close to the Ni-Sb distance that was determined for HP 6HB $Ba_3NiSb_2O_9$ from extended x-ray absorption fine structure data (2.68 Å) [21]. Furthermore, the O1-O1 distance within the common triangular face of the bi-octahedra (2.72 Å) is quite different from that observed for the Sb_2O_9 dimers in the AP 6HA form of $Ba_3NiSb_2O_9$ (2.59 Å) [22]. Another important result is that atomic coordinates, equivalent isotropic ADP, and mean bond distances compare well with those previously obtained from a satisfactory combined refinement of powder XRD and NPD data for the HP 6HB-like trigonal phase of $Ba_3NiSb_2O_9$ using the same centrosymmetric $P6_3/mmc$ starting model [23].

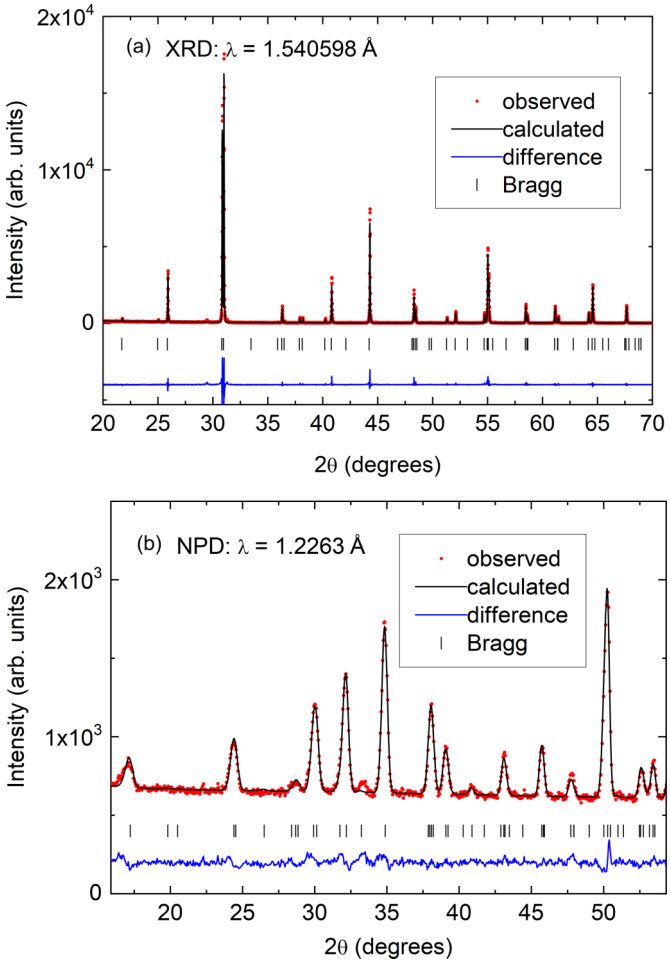

FIG. 3. Final combined Rietveld refinement plots of the (a) x-ray diffraction (XRD) and (b) neutron powder diffraction (NPD) data for $Ba_{2.5}Sr_{0.5}NiSb_2O_9$. Solid black curves are the best fits obtained with space group $P6_3/mmc$. The very weak Bragg reflections at $2\theta \approx 29.5^\circ$ (XRD) and 33° (NPD) were attributed to $Ba_3SrSb_2O_9$ impurity phase. Both portions of the observed diffraction profiles are shown for the same d-spacing range to illustrate that XRD and NPD data complement one another. Full patterns are shown in the Supplemental Material [30].

TABLE II. Principal bond lengths (Å) in $Ba_{2.5}Sr_{0.5}NiSb_2O_9$ derived from the joint refinement of x-ray and neutron diffraction data with space group $P6_3/mmc$. Mean bond distances reported for 6HB HP $Ba_3NiSb_2O_9$ in Ref. [23] are given in italics.

Ba1/Sr1-O1 × 4	2.888(3)	Sb2-O2 × 4	1.986(3)
Ba1/Sr1-O1 × 2	2.888(5)	Sb2-O2 × 2	1.986(4)
Ba1/Sr1-O2 × 6	2.922(3)	Mean Sb2-O2	1.986
Mean Ba1/Sr1-O	2.905		*(1.985)*
	(2.915)		
		Sb1/Ni1-O1 × 2	2.059(3)
Ba2/Sr2-O1 × 3	2.770(3)	Sb1/Ni1-O1 × 1	2.059(4)
Ba2/Sr2-O2 × 3	2.901(3)	Sb1/Ni1-O2 × 2	2.025(3)
Ba2/Sr2-O2 × 2	2.901(5)	Sb1/Ni1-O2 × 1	2.025(4)
Ba2/Sr2-O2 × 1	2.901(2)	Mean Sb1/Ni1-O	2.042
Ba2/Sr2-O2 × 3	3.073(3)		*(2.049)*
Mean Ba2/Sr2-O	2.911		
	(2.922)	Sb1/Ni1-Sb1/Ni1	2.659(3)
			(2.72)

To get information with a different spatial resolution, we investigated the structure of $Ba_{2.5}Sr_{0.5}NiSb_2O_9$ using PEDT on three different thin crystals harvested from the polycrystalline batch. The area probed by PEDT was $\sim 200 \times 200\,\mathrm{nm}^2$, as shown in Fig. 4. A detailed examination of PEDT patterns indicated a systematic absence of the odd-numbered $00l$ reflections. Although $00l$-odd reflections were observed on the [010] PEDT pattern because of multiple diffraction, they disappeared by slightly tilting the crystals [Fig. 4(b)], indicating that the actual symmetry of these crystals of AP $Ba_{2.5}Sr_{0.5}NiSb_2O_9$ cannot be trigonal $P3m1$ or $P3$, as it was suggested for HP 6HB $Ba_3NiSb_2O_9$ [23]. Our PEDT result stands in contrast to an earlier electron diffraction study of HP 6HB $Ba_3NiSb_2O_9$ which showed that its crystal structure cannot have hexagonal symmetry, although powder XRD and NPD patterns could be well refined in the hexagonal $P6_3/mmc$ triple-perovskite structure [23]. For $Ba_{2.5}Sr_{0.5}NiSb_2O_9$, refinements of the single-crystal PEDT intensities were conducted using the published $P6_3mc$ or $P6_3/mmc$ average structures of HP 6HB $Ba_3NiSb_2O_9$ as starting models [12,23]. Refined structural parameters and final agreement factors are given in the Supplemental Material

TABLE I. Refined structural parameters and final agreement factors for $Ba_{2.5}Sr_{0.5}NiSb_2O_9$ derived from x-ray and neutron diffraction data collected at 300 K.[a] Combined refinements of x-ray and neutron diffraction data were performed with centrosymmetric space group $P6_3/mmc$ (no. 194).

Atom	Site	x	y	z	U_{iso}(Å^2)	Occupancy
Ba1/Sr1	$2b$	0	0	$\frac{1}{4}$	0.0043(7)	Ba: 0.776(14)
						Sr: 0.224(14)
Ba2/Sr2	$4f$	$\frac{1}{3}$	$\frac{2}{3}$	0.09988(6)	0.0122(4)	Ba: 0.823(10)
						Sr: 0.177(10)
Sb2	$2a$	0	0	0	0.0044(1)	1
Sb1/Ni1	$4f$	$\frac{1}{3}$	$\frac{2}{3}$	0.65666(8)	0.0058(5)	Sb: 0.485(6)
						Ni: 0.515(6)
O1	$6h$	0.5094(4)	0.0189(8)	$\frac{1}{4}$	0.0148(7)	1
O2	$12k$	0.1630(4)	0.3259(7)	0.5797(1)	0.0129(5)	1

[a]Cell parameters: $a = 5.77206(2)$, $c = 14.24275(5)$. XRD: GOF = 1.54, Rp = 9.51, wRp = 13.52. NPD: GOF = 1.64, Rp = 2.30, wRp = 2.89. Overall: GOF = 1.56, Rp = 5.74, wRp = 6.16.

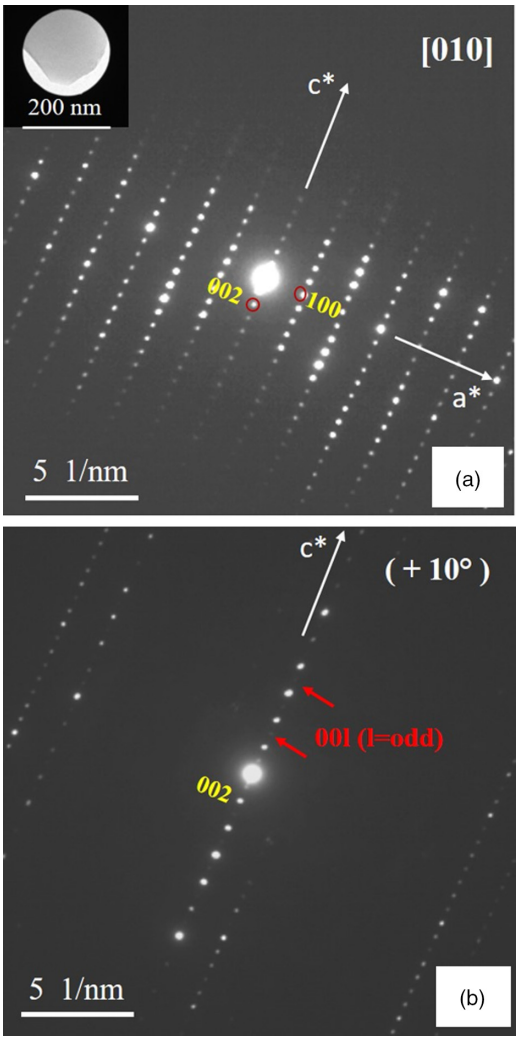

FIG. 4. (a) [010] precession electron diffraction tomography (PEDT) pattern for $Ba_{2.5}Sr_{0.5}NiSb_2O_9$. 00*l*-odd reflections are observed because multiple diffraction. Probed area is shown as an inset. (b) Tilted PEDT pattern (10° around c^*). Odd-numbered 00*l* reflections are missing.

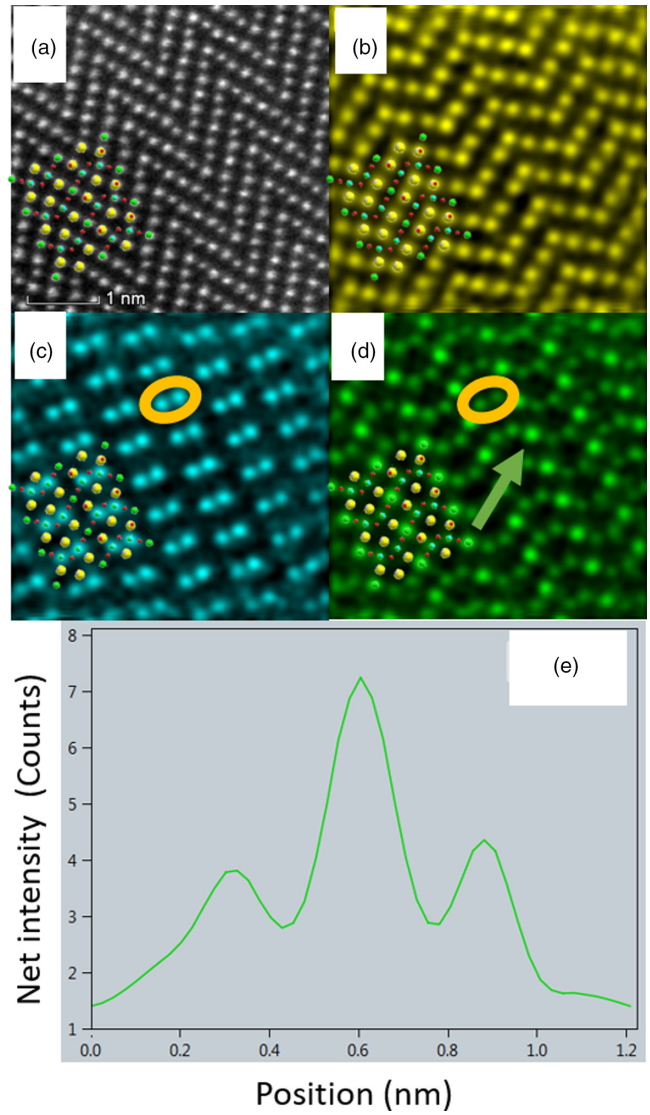

FIG. 5. High-angle annular dark field scanning transmission electron microscopy (HAADF-STEM) and energy dispersive x-ray spectroscopy (EDX) mapping for $Ba_{2.5}Sr_{0.5}NiSb_2O_9$ along the *b* axis with projections of the $P6_3/mmc$ structure derived from powder x-ray diffraction (XRD) and neutron powder diffraction (NPD). (a) HAADF-STEM image (20 mrad convergence angle, 91 mm camera length, 63–200 mrad collection angle range). EDX maps of (b) Ba, (c) Ni, and (d) Sb. Maps were obtained after Gaussian blur prefiltering and radial Wiener postfiltering with Velox software, Thermo Scientific. (e) Net intensity profile along the green arrow shown on the Sb map.

[30] (see Tables A4–A6). While both refinements yielded reasonable and comparable agreement factors, the low ADP value of Ni1 (2*b* site) obtained with the noncentrosymmetric space group $P6_3mc$ suggests a mixed Ni/Sb occupation of each of the two octahedral sites of the dumbbell. Structural parameters obtained using the centrosymmetric $P6_3/mmc$ model are in good agreement with those derived from XRD and NPD data (Table I).

Finally, $Ba_{2.5}Sr_{0.5}NiSb_2O_9$ was investigated by HAADF-STEM and EDX mapping (Fig. 5). A HAADF image viewed along the [010] axis is shown in Fig. 5(a). The intensity of HAADF images is a function of both the atomic number *Z*, approaching a Z^2 Rutherford-like relationship, and the projected thickness. Considering that the thickness does not vary significantly at such a scale, projections of the columns with the heavier atoms will appear brighter. This allowed us to superimpose the projection of the $P6_3/mmc$ structure derived from the joint refinement of x-ray and neutron diffraction data. To confirm the identification of the columns, EDX mapping was acquired for ∼ 40 min. Elemental maps of Ba, Ni, and Sb are presented in Figs. 5(b)–5(d). Columns containing Ni atoms also contain Sb atoms (see orange ovals), and intensity of columns containing only Sb atoms is much higher than those with both Sb and Ni. A net intensity profile performed in a direction perpendicular to three adjacent columns containing Sb atoms evidenced that brighter columns are twice as intense as the other ones [Fig. 5(e)]. This is consistent with site occupancies obtained from the $P6_3/mmc$ refinement of XRD and NPD data (Table I): 1 for Sb on the 2*a* site, $\frac{48}{52}$ for Sb/Ni

on the $4f$ site of the $NiSbO_9$ bi-octahedra. In other words, each column of $4f$ sites along the b axis contains roughly the same number of Ni and Sb atoms. Consequently, we did not observe a fully ordered all-up arrangement for the Ni-Sb dumbbells at the length scale of the crystal thickness along the [010] direction. For this direction of projection, it is however not possible to distinguish between complete disorder with random orientation of the dumbbells and a superimposition of several nanosized domains with nanoscale order in the orientation of the Ni-Sb dumbbells.

Several conclusions can be drawn from all these results. Judging from powder XRD and NPD, AP $Ba_{2.5}Sr_{0.5}NiSb_2O_9$ and HP 6HB $Ba_3NiSb_2O_9$ have very similar average structures that are typical of a hexagonal triple-perovskite containing $NiSbO_9$ face-sharing bi-octahedra (6HB phase). Their actual structures could however differ in terms of Ni-Sb dumbbell arrangement, which is different from the all-up long-range order depicted in Fig. 1(a) in both cases. Successful refinements of both our powder diffraction patterns and our PEDT data with the centrosymmetric $P6_3/mmc$ model strongly suggest the absence of long-range order for the Ni-Sb dumbbell arrangement. We note in passing that the same $P6_3/mmc$ structural model also provided a description of the average room temperature crystal structures of AP $Ba_3CuSb_2O_9$ based on single-crystal XRD data with a Cu/Sb ratio at the $4f$ position equal to unity [10]. For this latter compound, which contains Jahn-Teller active Cu^{2+} ions, further investigations indicated nanoscale Cu-Sb dumbbell honeycomblike ordering [10,20]. In HP 6HB $Ba_3NiSb_2O_9$, it was suggested that polycrystalline samples contain ordered domains of small dimensions (1–10 nm), having a trigonal structure like the one shown in Fig. 1(b) without the 6_3 axis and the c glide plane of the $P6_3/mmc$ hexagonal unit cell [23]. In this scenario, Rietveld refinements of XRD and NPD patterns give a centrosymmetric $P6_3/mmc$ average structure over many domains. These domains were not observed in the HAADF-STEM image obtained along the b axis for HP 6HB $Ba_3NiSb_2O_9$, and it was therefore assumed that this image was obtained from a crystallite that contained several domains throughout its thickness [23]. Even if we did not observe either the trigonal symmetry in thin crystals or regions with coaligned dumbbells on our HAADF-STEM images projected along the b axis, chemical correlations for the Ni-Sb dumbbell arrangement may exist in our samples of $Ba_{2.5}Sr_{0.5}NiSb_2O_9$, too. Such chemical correlations would however be different in nature from those suggested for HP 6HB $Ba_3NiSb_2O_9$ because the trigonal symmetry, which is compatible with up-down-up-down correlations for the dumbbell arrangement along the stacking c axis, was not observed in thin crystals of $Ba_{2.5}Sr_{0.5}NiSb_2O_9$.

2. 3C $Ba_{1.75}Sr_{1.25}NiSb_2O_9$ ($x = 1.25$)

Table III shows the refined structural parameters and final reliability factors obtained for $Ba_{1.75}Sr_{1.25}NiSb_2O_9$. Our starting point for the structure refinement was the published $Fm\bar{3}m$ crystal structure of the 3C HP phase of $Ba_3NiSb_2O_9$ [12]. Within this model, a $Ba_{3-x}Sr_xNiSb_2O_9$ structure is described as a (Ba, Sr)$_2BB'O_6$ double perovskite ($Ba_{(6-2x)/3}Sr_{2x/3}Ni_{2/3}Sb_{4/3}O_6$), where B and B' octahedral sites are occupied by Sb and ($\frac{2}{3}$Ni + $\frac{1}{3}$Sb) atoms, respectively (Fig. 2). Ni and Sb atoms are randomly distributed at the B' site [12]. Rock salt ordering of B/B' cations is a common occurrence in $A_2BB'O_6$ double perovskites [34,35]. Using this starting model, a satisfactory combined refinement of our XRD and NPD data was obtained. Maximum and minimum electron densities in the difference Fourier map were 0.74 and −0.38 electron Å^{-3}, respectively. Figure 6 shows the final Rietveld plots. There was no sign of additional structural periodicities. Atomic coordinates and isotropic ADP were kept identical for Ba and Sr atoms at the Wyckoff 8c site, and for Ni and Sb atoms at the Wyckoff 4b site. Crystallographic sites were all assumed to be fully occupied, and site occupancies were refined for the Ba/Sr(8c) and Ni/Sb(4b) sites. It yielded cationic ratios close to the nominal ones: Sr/Ba ≈ 0.66(2) (vs nominal 0.71) and Ni/Sb ≈ 1.92(3) at the 4b site (vs nominal 2.0). The only refined atomic coordinate, namely, $x = 0.2533(1)$ for the O atom at the Wyckoff 24e position, is close to the one determined from powder XRD data for HP 3C $Ba_3NiSb_2O_9$, $x = 0.2409(8)$ [12]. The mean Sb-O bond length around the 4a site, 1.9928(9) Å, is close to the values reported for the SbO_6 octahedron in the double perovskite structure of $Sr_3NiSb_2O_9$ (1.99–2.01 Å) [36,37]. The latter compound ($x = 3$) is prepared at AP using a high-temperature solid-state reaction method like that used for $Ba_{1.75}Sr_{1.25}NiSb_2O_9$. The mean Ni/Sb-O bond distance around the 4b site is 2.0454(9) Å, which is like the value of 2.03 Å found for the $(Ni_{2/3}Sb_{1/3})O_6$ octahedron in $Sr_3NiSb_2O_9$ [37]. The mean Ba/Sr-O bond length of 2.85556(2) Å compares well with both the mean Sr-O distance of 2.82 Å observed in $Sr_3NiSb_2O_9$ [37] and the Ba-O distance calculated from ionic radii (3.01 Å).

TABLE III. Refined structural parameters and final agreement factors for 3C $Ba_{1.75}Sr_{1.25}NiSb_2O_9$ derived from x-ray and neutron diffraction data collected at 300 K.[a] Refinements were performed using a $Fm\bar{3}m$ (no. 225) double perovskite in a $A_2BB'O_6$ model with $A(8c) = Ba_{0.583}Sr_{0.417}$, $B(4a) = Sb$, and $B'(4b) = Ni_{2/3}Sb_{1/3}$ as a starting model.

Atom	Site	x	y	z	U_{iso}(Å^2)	Occupancy
Ba/Sr	8c	$\frac{1}{4}$	$\frac{1}{4}$	$\frac{1}{4}$	0.0104(1)	Ba: 0.601(5) Sr: 0.399(5)
Sb	4a	$\frac{1}{2}$	$\frac{1}{2}$	$\frac{1}{2}$	0.0032(2)	1
Ni/Sb	4b	0	0	0	0.0031(2)	Ni: 0.658(3) Sb: 0.342(3)
O	24e	0.2533(1)	0	0	0.01262(7)	1

[a]Cell parameters: $a = 8.07640(3)$. XRD: GOF = 1.42, Rp = 9.12, wRp = 14.14. NPD: GOF = 3.76, Rp = 3.39, wRp = 4.57. Overall: GOF = 1.99, Rp = 4.86, wRp = 5.82.

B. Magnetization and heat capacity

Figure 7 shows the temperature-dependent magnetic susceptibility $\chi(T)$ of 6H $Ba_{2.5}Sr_{0.5}NiSb_2O_9$ and 3C $Ba_{1.75}Sr_{1.25}NiSb_2O_9$. These two phases will be hereafter referred to as 6H-Sr and 3C-Sr, respectively. Previously obtained data for 6HB and 3C phases of pure $Ba_3NiSb_2O_9$ [12,24] synthetized under HP, termed 6HB-HP and 3C-HP

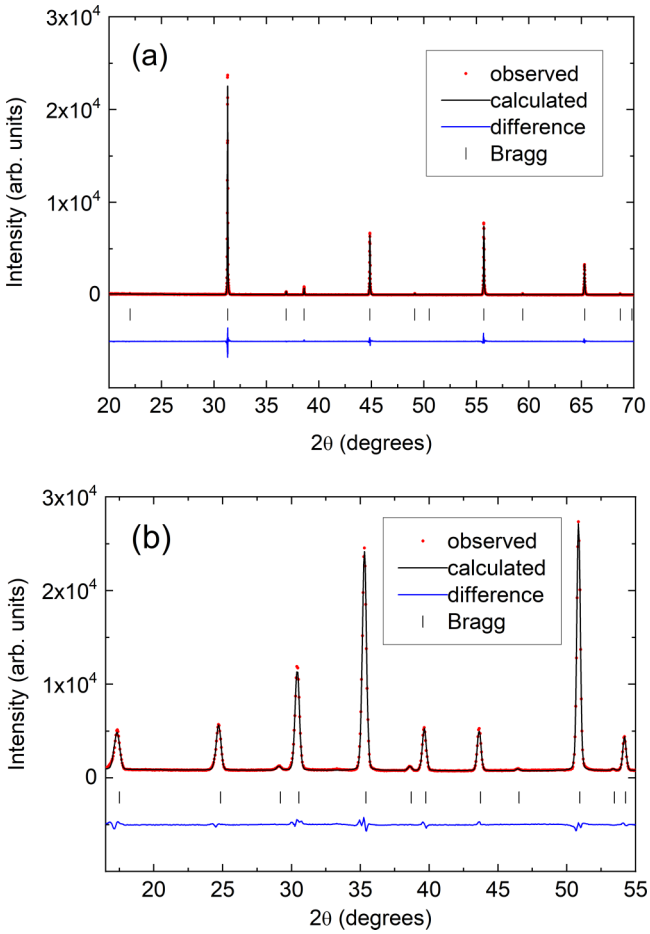

FIG. 6. Final combined Rietveld refinement plots of the (a) x-ray diffraction (XRD; $\lambda = 1.540598$ Å) and (b) neutron powder diffraction (NPD) data ($\lambda = 1.2247$ Å) for 3*C* $Ba_{1.75}Sr_{1.25}NiSb_2O_9$. Both portions of the observed diffraction profiles are shown for the same *d*-spacing range to illustrate that XRD and NPD data complement one another. Full patterns are shown in the Supplemental Material [30].

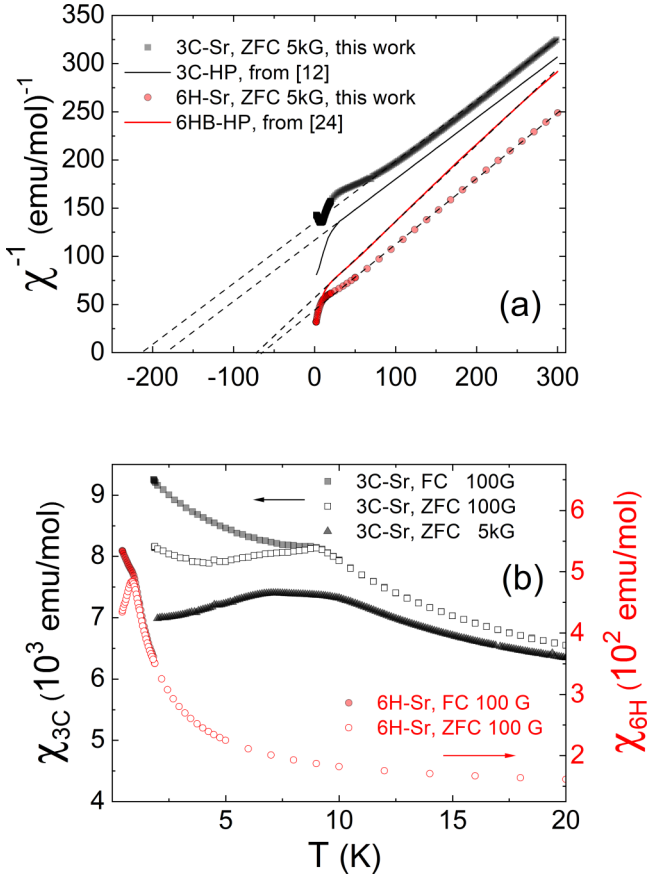

FIG. 7. (a) Inverse magnetic susceptibility χ^{-1} vs temperature T for our samples of $Ba_{2.5}Sr_{0.5}NiSb_2O_9$ (6*H*-Sr) and of $Ba_{1.75}Sr_{1.25}NiSb_2O_9$ (3*C*-Sr) compared with 6HB and 3*C* phases of $Ba_3NiSb_2O_9$ synthesized under high pressure (6HB-HP and 3*C*-HP) [12,24]. (b) Low-T susceptibility of 6*H*-Sr and 3*C*-Sr samples.

below, are also shown in Fig. 7(a) for comparison. The Weiss temperatures and effective moments as extracted from the high-T plot of χ^{-1} vs T are listed in Table IV. The Weiss temperatures of the 6*H*-Sr ($\Theta_{\text{Weiss}} \approx -65$ K) and 3*C*-Sr ($\Theta_{\text{Weiss}} \approx -213$ K) phases reflect dominant antiferromagnetic spin-spin interactions whose magnitudes are like those observed in the HP phases of pure $Ba_3NiSb_2O_9$.

For the 6HB-HP phase of $Ba_3NiSb_2O_9$, no field-cooled (FC)-zero-field cooled (ZFC) splitting was observed for the susceptibility measured under a field of 5 kG down to 2 K [12]. We know of no ZFC-FC data acquired under a lower field value for 6HB-HP. Spin-liquid behavior was confirmed through μSR and NMR experiments, with a leveling off of the local susceptibility below 50 K as measured through the shift of the ^{121}Sb NMR line [24]. The upturn in ZFC-$\chi(T)$ measured at 5 or 1 kG was analyzed by introducing an additional Curie component corresponding to $\sim 2\%$ of $S = 1$ orphan spins [12,24]. The variable-temperature ZFC magnetic susceptibility measured at 5 kG for 6*H*-Sr $Ba_{2.5}Sr_{0.5}NiSb_2O_9$ is comparable with the published data for 6HB-HP, showing a similar Curie tail at low temperature. For an applied field of 100 G, the 6*H*-Sr compound displays a clear opening between the ZFC and FC branches at 0.95(15) K and a maximum in the ZFC trace [Fig. 7(b)]. μSR experiments described in the next section show, however, that this opening does not arise from a bulk magnetic transition, e.g., a spin-glass transition. As can be seen in Fig. 8, magnetization measurements performed at 0.450 K can be analyzed using a combination of a nonsaturated linear term and a term corresponding to $\sim 2\%$ orphan spins, like in the 6HB-HP phase.

TABLE IV. Values of the effective Ni moments and Weiss temperatures for 6*H* $Ba_{2.5}Sr_{0.5}NiSb_2O_9$ (6*H*-Sr) and 3*C* $Ba_{1.75}Sr_{1.25}NiSb_2O_9$ (3*C*-Sr) compared with existing data for the phases of pure $Ba_3NiSb_2O_9$ obtained under high pressure (6HB-HP and 3*C*-HP).

Phase	Synthesis	μ_{eff} (μ_B/Ni)	Θ_{Weiss} (K)	Reference
6*H*	6HB-HP	~3.54	−75.6(6)	[12]
		3.29(2)	−73(2)	[24]
	6*H*-Sr	3.43(2)	−65(1)	This paper
3*C*	3*C*-HP	~3.54	−182.5(3)	[12]
	3*C*-Sr	3.55 (2)	−213(2)	This paper

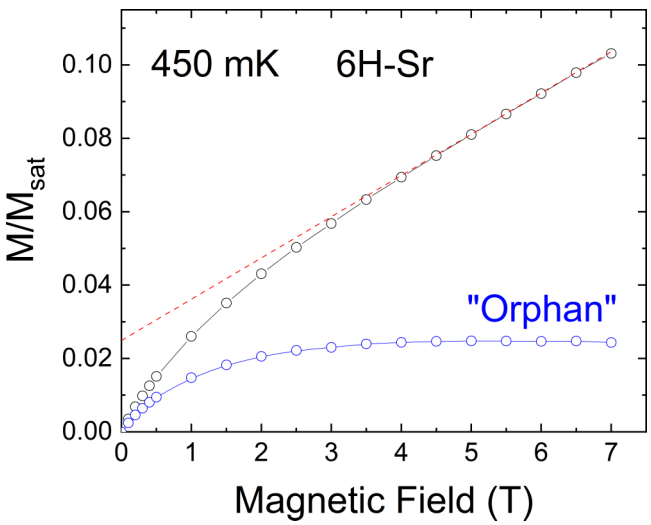

FIG. 8. Magnetization M plotted as M/M_{sat} vs applied field at 450 mK for $Ba_{2.5}Sr_{0.5}NiSb_2O_9$ (6H-Sr). The saturation magnetization $M_{\text{sat}} \propto gS\mu_B$ was calculated using $S = 1$ and $g = 2.4$. The fit (red line) is the combination of a linear term and a Brillouin function for a spin 1 (orphan contribution).

For the 3C phases, our susceptibility results for 3C-Sr $Ba_{1.75}Sr_{1.25}NiSb_2O_9$ show low-T behavior which differs notably from that reported in Ref. [12] for 3C-HP $Ba_3NiSb_2O_9$. The ZFC susceptibility curve $\chi(T)$ measured under a field of 5 kG displays two changes of slope at $\sim$ 10 and 6 K [Fig. 7(b)], which were absent in 3C-HP $Ba_3NiSb_2O_9$. Furthermore, a FC-ZFC bifurcation occurs in the susceptibility data below 9 K for applied fields up to 10 kG, combined with a sample-dependent small Curie upturn of the susceptibility. To provide further insight, the magnetic specific heat $C_M(T)$ of 3C-Sr $Ba_{1.75}Sr_{1.25}NiSb_2O_9$ was also measured. It features a broad maximum at 12 K, as shown in Fig. 9, slightly higher than

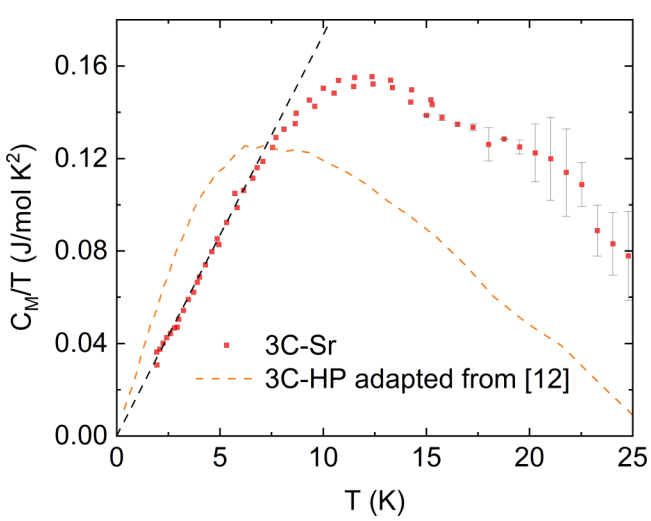

FIG. 9. Magnetic specific heat plotted as C_M/T vs temperature T for $Ba_{1.75}Sr_{1.25}NiSb_2O_9$ (3C-Sr). The straight dashed line is the fit $C_M = \gamma T^2$ with $\gamma \sim 1.7 \times 10^{-2}$ J/mol K^3. The dashed-curve represents the results from Ref, [12] for the 3C-HP phase of $Ba_3NiSb_2O_9$ synthesized under high pressure.

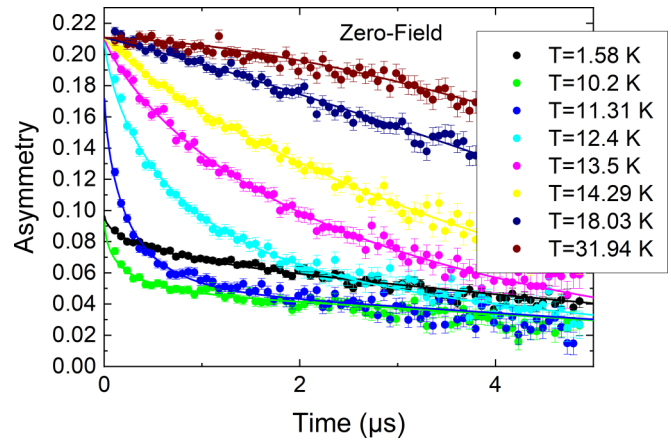

FIG. 10. Muon decay asymmetry in zero applied field in 3C $Ba_{1.75}Sr_{1.25}NiSb_2O_9$ (3C-Sr). Lines are fits described in the text.

both the FC-ZFC splitting and the changes of slope in the susceptibility curves. Our C_M/T data substantially differ from the data for 3C-HP $Ba_3NiSb_2O_9$ from Ref. [12], for which a broad maximum was also reported but at a lower temperature of $\sim$ 8 K. The magnetic total entropy is also found larger here, 40% instead of 22% of Rln(3) per $S = 1$ spin. At low T, between 2 and 7 K, quadratic behavior of the specific heat is found $C_M \sim 1.7 \times 10^{-2}$ T^2 J mol^{-1} K^{-1}. Similar quadratic behavior of $C_M(T)$ was observed for 3C-HP $Ba_3NiSb_2O_9$ between 0.35 and 5 K but with a larger slope.

C. μSR and ^{121}Sb NMR

To reveal the intrinsic properties of the two 6H-Sr and 3C-Sr phases, we have further performed local probe μSR and NMR experiments.

1. 3C $Ba_{1.75}Sr_{1.25}NiSb_2O_9$ (3C-Sr)

We performed both μSR and NMR measurements on the very same sample of the 3C-Sr phase, and they gave a consistent picture, as detailed below. Figure 10 shows the muon decay asymmetry in ZF for different temperatures down to 1.6 K. The dramatic increase of the early time relaxation rate around 11 K and the larger weight of the long-time tail at low temperature are typical signatures of a magnetic transition from paramagnetism to static magnetism in the ground state. Accordingly, the asymmetry at long time $t > 0.1\ \mu$s could be fitted on the whole T range to

$$a(t) = (a_0 - a_p)\Big\{(1-f)\exp[-(\sigma t)^2]\exp[-(\lambda t)^\beta] + \frac{f}{3}\exp[-(\lambda_f t)^{1/2}]\Big\} + a_p\exp[-(\sigma t)^2]\exp(-\lambda_p t),$$

where $a_0 = 0.21$ is the initial asymmetry, and $a_p/a_0 = 0.2$ is a fraction of the muon sites which do not sense any frozen field, e.g., surrounded by Sb's only and kept unchanged at all temperatures. The fraction f stands for the volume fraction of the 3C-Sr phase that undergoes the magnetic transition. Above 12.4 K, f is set to 0, and the relaxation is both due to static nuclear moments, yielding the Gaussian decay term ($\sigma = 0.11\ \mu$s^{-1}), and fluctuations of the electronic moments,

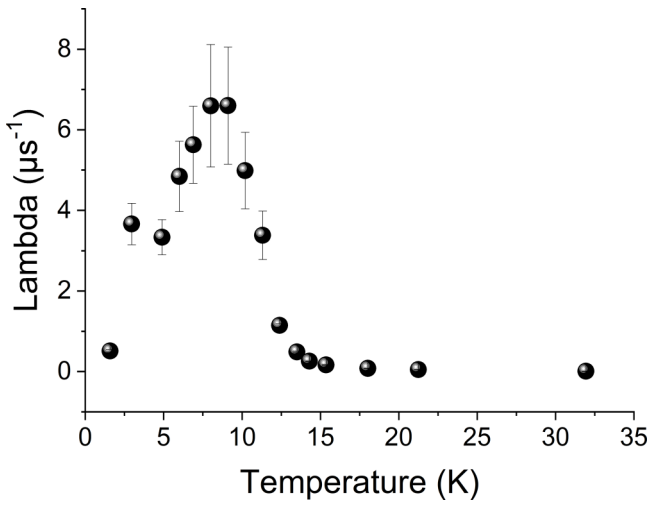

FIG. 11. Temperature evolution of the relaxation rate in 3*C* $Ba_{1.75}Sr_{1.25}NiSb_2O_9$. The plotted rate is λ above 12.4 K, λ_f below 10.2 K and a weighted average $f\lambda_f + (1-f)\lambda$ at $T = 11.3$ K.

yielding the roughly exponential decay term $\exp[-(\lambda t)^\beta]$ ($0.7 < \beta < 1$). The relaxation rate λ increases gradually, as shown in Fig. 11, upon cooling toward the magnetic transition temperature. Below 10.2 K, f could be set to 1, i.e., static magnetism has developed in the whole sample volume except for the a_p fraction. In the $t > 0.1$ μs time window shown, only the slow relaxation of the expected $\frac{1}{3}$ rd tail, corresponding to muon spins aligned with the internal fields, is detected, while the fast relaxing $\frac{2}{3}$ rd component of the frozen signal is missing (this component is discussed further below). The exponent $\frac{1}{2}$ of the stretched exponential relaxation $\exp[-(\lambda_f t)^{1/2}]$ in this regime points to a wide distribution of relaxation rates and the possibility of a disordered ground state. Close to the transition, for $T = 11.3$ K, both static and dynamical fractions contribute, and the best fit to the data gives $f = 0.30(1)$. The relaxation rate shows a well-defined but rather broad peak around 8.5(5) K, substantially below the magnetic transition 11(1) K temperature, suggesting unusual magnetic excitations.

The early time relaxation ($t < 0.25$ μs) is presented at various temperatures below the transition on Fig. 12. A strongly damped spontaneous oscillation in zero applied field is clearly visible at low temperature which discards a spin-glass scenario where only one dip in the asymmetry would be expected. It gives evidence for a magnetically long-range ordered ground state albeit with substantial disorder in line with the square root exponential relaxation discussed above in the same T range. The early time relaxation was fitted to

$$a(t) = a_s\left\{\tfrac{1}{3} + \tfrac{2}{3}\cos(2\pi\nu_s t + \varphi)\exp[-(\sigma_s t)^2]\right\} \times \exp(-\lambda_{\rm osc} t) + a_b\left\{\tfrac{1}{3} + \tfrac{2}{3}\exp[-(\sigma_b t)^2]\right\} \times \exp(-\lambda_b t) + a_p,$$

with the constraint $a_s + a_b + a_p = a_0$. The second term accounts for the initial Gaussian-like relaxation, likely arising from too fast and too damped oscillations to be detected. The first oscillating term gives the frequency ν_s of the spontaneous

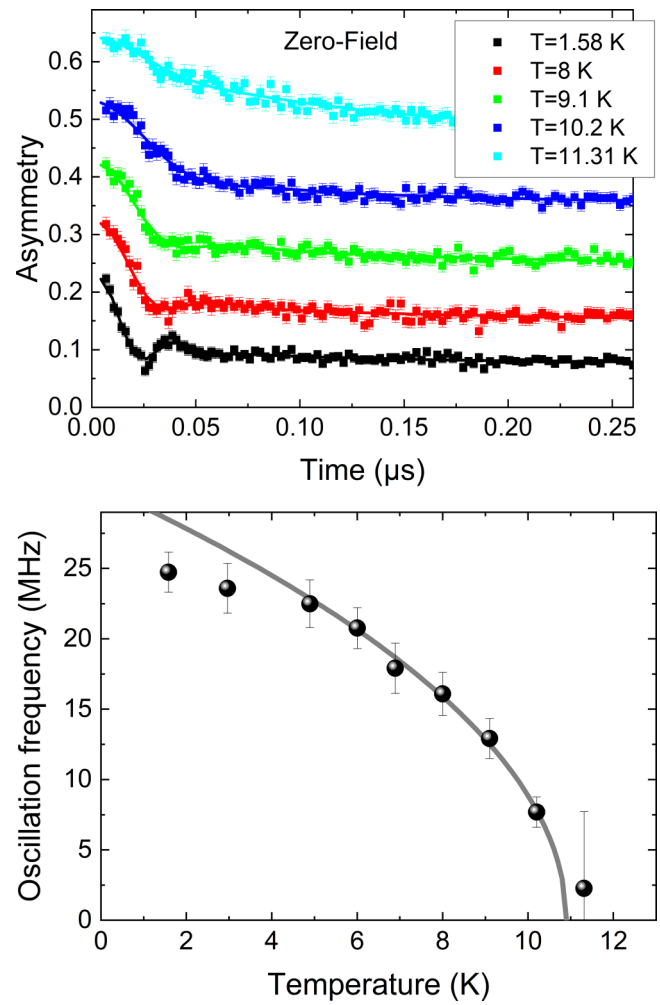

FIG. 12. Top: Early time muon decay asymmetry in zero field in 3*C* $Ba_{1.75}Sr_{1.25}NiSb_2O_9$ (3*C*-Sr) at selected temperatures below the transition. For clarity, the spectra are shifted vertically by $\Delta a = 0.1$ from each other. Lines are fits described in the text. Bottom: Temperature evolution of the damped oscillation frequency extracted from the fits in the upper panel. The line is a plot of $A\sqrt{1-T/T_N}$ with $A = 30.8$ MHz and $T_N = 10.9$ K.

oscillation which is plotted in the lower panel of Fig. 12. The precession of the muon spin in ZF is a direct signature of the presence of an internal field $B_{\rm int} = 2\pi\nu_s/\gamma$ at the muon stopping where $\frac{\gamma}{2\pi} = 135.5$ MHz/T is the muon gyromagnetic ratio. Therefore $\nu_s(T)$ represents the order parameter in the magnetic phase.

We now detail our ^{121}Sb NMR measurements which confirm the presence of a static ordering below 11(1) K. In Fig. 13(c), some typical spectra taken in the 1.2–60 K range are displayed for the 3*C*-Sr sample. A progressive broadening occurs, as reported in Fig. 13(b), with decreasing temperatures in the T range 60–12 K. It is the hallmark of a distribution of local fields which can be either assigned to a distribution of Ni susceptibilities or a distribution of hyperfine couplings of the ^{121}Sb nuclei to the surrounding Ni's. Most strikingly, the intensity of our signal dramatically decreases around 10 K, where a marked kink occurs in the susceptibility data [Fig. 13(a)] taken under a 5 kG field. The loss of intensity

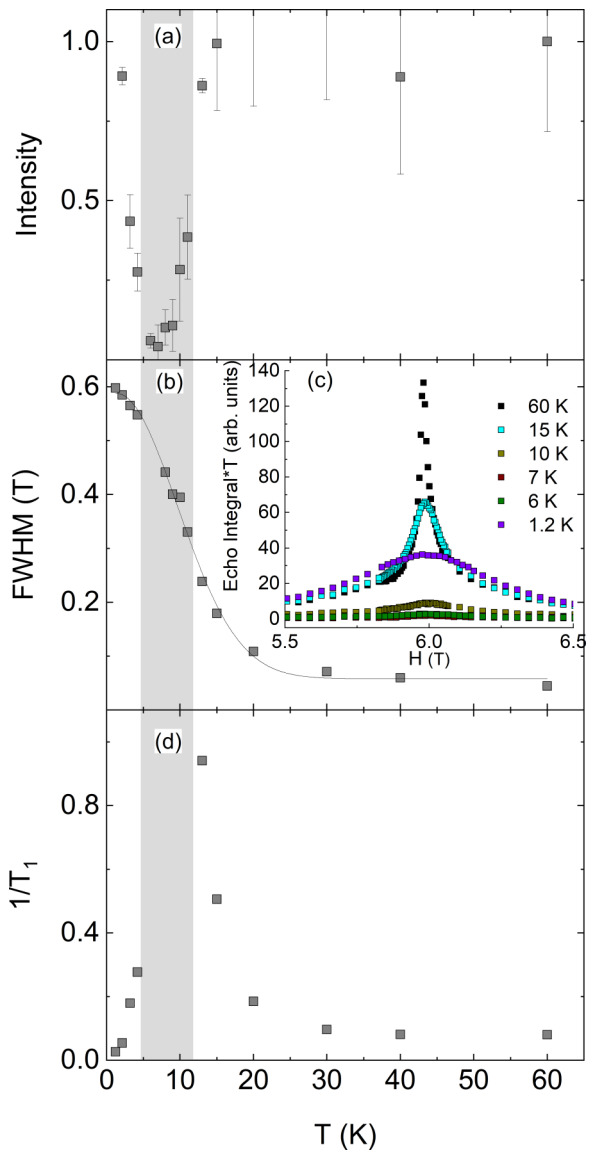

FIG. 13. ^{121}Sb nuclear magnetic resonance (NMR) data for 3C $Ba_{1.75}Sr_{1.25}NiSb_2O_9$: (a) Integrated spectral intensity corrected by T_2 relaxation effects: it represents the normalized number of detected nuclei. The gray area signals the T range where only a weak intensity is detected; therefore, the NMR spectra reflect only a minority of sites harboring the longest T_2' s. (b) Full width measured at half maximum for all spectra from 60 to 1.2 K. (c) Plot of typical ^{121}Sb NMR spectra obtained by sweeping the field at a fixed frequency of 61.148 MHz. The signal is hardly observable around 10 K. (d) Divergence of the longitudinal relaxation rate $1/T_1$ signaling a magnetic transition.

results from a distribution of relaxation times, a large part of which becomes shorter than the 10 µs lower limit of the NMR time window [38,39]. This increase of the transverse relaxation rate can be safely assigned to a slowing down of the fluctuations in the context of a phase transition, also evident through the $1/T_1$ divergence [Fig. 13(d)].

From the scaling of the shift with the susceptibility between 80 and 300 K (not shown), we could extract a hyperfine constant of 3.43 (10) kOe/μ_B. In the case of perfect ordering with a well-defined value of the internal field in a powder sample, one expects a rectangular line shape, with a full width equal to twice the internal field at the Sb site. On the contrary, the line shape observed here has a Lorentzian shape, reflecting a distribution of internal fields and thus a substantial amount of disorder in the frozen phase. The half width at half maximum of 0.3 T indicates a subsequent freezing with a moment value of 0.87(3) μ_B. This is also in line with the low value of $1/T_1$ found in our relaxation measurements at 1.2 K, showing that there is no or very little persistent fluctuations as expected for conventional magnetic phases. All these results perfectly match the μSR results.

2. 6H $Ba_{2.5}Sr_{0.5}NiSb_2O_9$ (6H-Sr)

For the 6H-Sr phase, the NMR transverse relaxation times T_2 are extremely short, which prohibits the drawing of firm conclusions, as discussed in Ref. [24] for the 6HB-HP phase of $Ba_3SrNiSb_2O_9$, especially at low T, which is our main focus here.

The μSR relaxation measured in a powder sample of the 6H-Sr compound is in marked contrast to the 3C-Sr case described above, see Fig. 14. Although an increase of the relaxation rate is similarly observed upon cooling the sample, it remains moderate and nearly T independent below 1 K. Note also that, at variance with the 3C-Sr case, there is no crossing of the asymmetry curves, thus no development of a $\frac{1}{3}$rd tail at low temperature, which would be characteristic of the presence of static internal fields. This discards a spin-glass ground state and suggests a dynamical behavior of the 6H-Sr phase across the whole temperature range, down to 95 mK, the lowest temperature in this paper. This was also the case in the 6HB-HP pure compound [24]. Therefore, the absence of static magnetism at $T \to 0$ K, a first hint at a spin-liquid ground state, seems to be a robust feature of the 6H phases having Ni-Sb dumbbells, whatever the synthesis route used to stabilize it. There are nonetheless interesting differences in μSR between the 6HB-HP and 6H-Sr materials that we investigate below in detail.

At variance with the 6HB-HP counterpart where the relaxation remains exponential at all temperatures, there is a clear evolution in the form of the μSR signal in the 6H-Sr sample from exponential at high temperatures to Gaussian at low T (see Fig. 14, upper panel). In the usual dynamical Kubo-Toyabe (DKT) model [40], the Gaussian shape at low T implies very slow fluctuations at the verge of static magnetism. To quantify this effect, we fitted the relaxations to

$$a(t) = a_0 G(t, \nu, \Delta, B_L) + a_{bkg},$$

where $G(t, \nu, \Delta, B_L)$ is the function introduced in Ref. [41] to approximate the DKT model in the fluctuating regime, i.e., if the fluctuation frequency ν is larger than the width of the distribution of fluctuating internal fields, Δ. We could get reasonable fits of the data at all temperature with this model function with no applied field and with ν as the only variable parameter. The temperature evolution of ν is shown in the inset of Fig. 15. As expected from the shape of the relaxation, the fluctuations slow down drastically, by ~ 2 orders of magnitude, from high to low T. At base T, $\nu/\Delta \sim 1.6$ which is indeed close to static magnetism ($\nu/\Delta = 1$). For such slow fluctuations, we expect that a longitudinal field $B_L \gg \Delta/\gamma = 9.2(1)$ G applied along the initial muon spin direction should

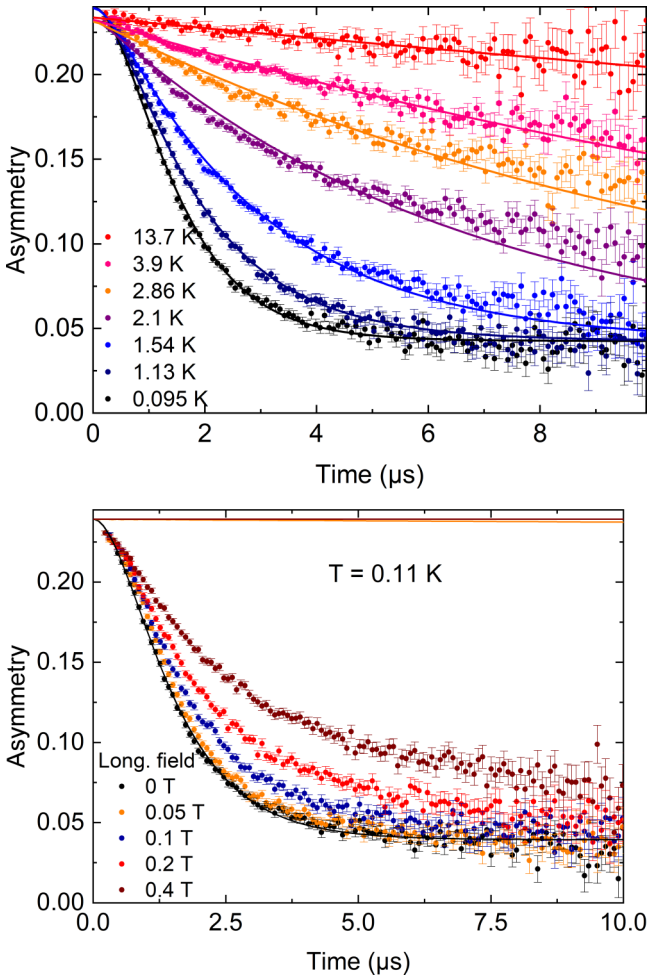

FIG. 14. Top: Muon decay asymmetry in a small 0.002 T field applied parallel to muon beam polarization to decouple small nuclear fields in 6H-Sr $Ba_{2.5}Sr_{0.5}NiSb_2O_9$ at various temperatures. Lines are fits described in the text. Bottom: Muon decay asymmetry with an applied longitudinal magnetic field. The nearly flat orange and brown lines show the expected relaxation at 0.05 and 0.4 T from the model used to fit the zero-field data (black line).

dominate the total field probed by the muons and suppress the relaxation, as shown by the simulations in the lower panel of Fig. 14 for $B_L = 0.05$ and 0.4 T, respectively. However, for such applied fields, the experimental relaxation remains surprisingly large, pointing to much stronger spin fluctuations than anticipated from the Gaussian relaxation shape. Such an undecouplable Gaussian shape, observed previously in some highly frustrated magnets [42–44], remains mysterious to date but certainly suggests exotic spin dynamics in this $S = 1$ triangular compound.

To compare with the ZF relaxation rate obtained in the 6HB-HP pure counterpart from exponential fits [24], we used the fast fluctuation approximation $G(t, \nu, \Delta, B_L = 0) \simeq \exp(-2\Delta^2 t/\nu)$, and we plotted $\lambda = 2\Delta^2/\nu$ for the 6H-Sr case in Fig. 15. The slowing down of the spin fluctuations in the 6H-Sr compound shifted to a significantly lower temperature (typically 2.4 times lower) than in the 6HB-HP pure one. We note that this difference cannot be explained by the much smaller change in the magnetic interactions in the two

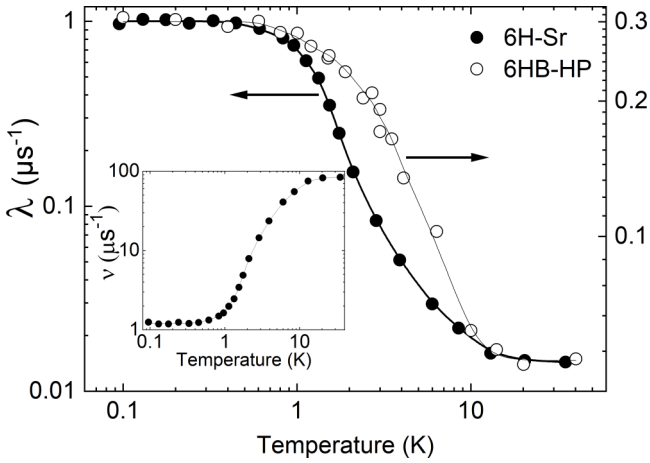

FIG. 15. Inset: Temperature dependence of the fluctuation rate ν obtained from the fits of the zero-field relaxation shown in Fig. 14 (upper panel). Main panel: Comparison of the temperature dependence of the relaxation rates $\lambda \propto 1/\nu$ in the 6HB-HP $Ba_3SrNiSb_2O_9$ (from Ref. [24]) and 6H-Sr $Ba_{2.5}Sr_{0.5}NiSb_2O_9$ (this paper) phases.

variants. Indeed, both compounds show similar Curie-Weiss temperatures (see Table IV).

IV. DISCUSSION

We first explain why both Ba/Sr substitution and physical pressures lead to the same 6H with Sb_2O_9 pairs → 6H with $NiSbO_9$ pairs → 3C sequence of structural phases in $Ba_3NiSb_2O_9$. The substitution of Sr^{2+} for Ba^{2+} in $Ba_3NiSb_2O_9$ causes the Goldschmidt tolerance factor to decrease. In a perovskitelike ABO_3 oxide, the tolerance factor can be written as $t = \frac{(r_A+r_O)}{\sqrt{2}(r_B+r_O)}$ where r_A and r_B are the average radii of the A and B sites, respectively, and r_O is the radius of oxide ion [45]. Hexagonal 6H structures, which can accommodate large A cations and short B-B distances in pairs of face-sharing octahedra, are observed when $t > 1$. For $t \cong 1$, 3C structures with cubic symmetry occur. Distortions to lower symmetries are expected when the A-site cation becomes too small for the cubo-octahedral cavities, i.e., when t decreases further [46]. For $Ba_{3-x}Sr_xNiSb_2O_9$, also written as $[Ba_{(3-x)/3}Sr_{x/3}][Ni_{1/3}Sb_{2/3}]O_3$, the tolerance factor calculated using Shannon's ionic radii [25] decreases from $t = 1.048$ in AP 6HA $Ba_3NiSb_2O_9$ ($x = 0$) to $t = 0.989$ in the double perovskite $Sr_3NiSb_2O_9$ ($x = 3$) and is equal to 1.039 and 1.024 for 6H-Sr $Ba_{2.5}Sr_{0.5}NiSb_2O_9$ and 3C-Sr $Ba_{1.75}Sr_{1.25}NiSb_2O_9$, respectively. In the 3$C$-type region, the crystal structure evolves from cubic (space group $Fm\bar{3}m$) for $x = 1.25$ to monoclinic (space group $P2_1/n$) for $x = 3$. Other perovskite-related oxides experience similar structural changes as the tolerance factor decreases. For instance, partial substitution of Sr for Ba in $Ba_3ZnTiWO_9$ ($t = 1.039$) destabilizes the 6H crystal structure, and the Sr substituted compound with $t = 1.027$ forms in the 3C cubic structure [47]. Also, a sequence of phases $Fm\bar{3}m \rightarrow I4/m \rightarrow I2/m \rightarrow P21/n$, which are associated with the introduction of cooperative tilting of the corner-sharing octahedra, has been reported for double perovskite systems with increasing Ba/Sr substitution rates [26,28]. Similar trends are observed as the

physical pressure increases because pressure tends to decrease the tolerance factor if the A-site cations are more compressible than the B-site ions in the ABO_3 oxide [48]. This explains why both chemical and physical pressures lead to the same sequence of structural phases in $Ba_3NiSb_2O_9$ which contains large and compressible Ba^{2+} on the A site.

Although the average structures of 6H-Sr $Ba_{2.5}Sr_{0.5}NiSb_2O_9$ and 6HB-HP $Ba_3NiSb_2O_9$ are described using the same $P6_3/mmc$ model, electron diffraction results (this paper and Ref. [23]) suggest that their actual crystal symmetries are different. This difference, which cannot be explained based on the t factor alone, is probably associated with different Ni-Sb dumbbell arrangements and indicates that the substitution-induced chemical pressure is not equivalent to the HP-HT treatment with relaxed physical pressure. In this respect, we note that the 6H-Sr phase prepared at AP conditions is expected to be thermodynamically stable, while perovskite oxides produced at HP can be metastable at AP and room temperature [48].

We now turn to the magnetic properties of the 6H-Sr phase $Ba_{2.5}Sr_{0.5}NiSb_2O_9$. Thermodynamic and μSR results obtained earlier for pure 6HB-HP [12,24] and presented here for the AP 6H-Sr phase display qualitatively similar behaviors, albeit with some small differences. The absolute value of the Weiss temperature is slightly smaller; the effective moment is comparable with those previously found for the HP 6HB phase. Although still poorly understood, the μSR relaxation plateau attributed to persistent dynamics has long been taken as a hallmark of spin-liquid behavior. We notice that the latter occurs at lower temperature for the AP 6H-Sr sample. It is reasonable to think that these small differences result from some Sr-induced additional disorder and a slightly modified and perhaps more complex scheme of interactions, as commented on below. We note that a previous neutron study [29] did not find—within the accuracy of the 6HB-HP data—any difference between the two 6H phases and gave evidence for shallow maxima in the structure factor $S(q)$ at arbitrary positions in the Brillouin zone for a triangular lattice. The results approached the predictions for a $U(1)$ gapless QSL state for $S = 1$ on the triangular lattice but failed to reproduce the position of the maxima at the K-points of the Brillouin zone. From the study by Cheng *et al.* [12], the observed T-linear specific heat as $T \to 0$ is also an important result which altogether with the NMR study of the 6HB-HP phase led to the conclusion of a gapless spin-liquid ground state [24]. Several interpretations of the NMR data were discussed within (i) the triangular model incorporating biquadratic, next-nearest neighbor (NNN), and interlayer exchanges as well as single-ion anisotropy, which did not reproduce the gapless $1/T_1$ and the line shapes from the experiments, or (ii) a J_1-J_2 honeycomb buckled model, which will be discussed below in light of theoretical progress accomplished since then. The microscopic origin of this QSL state was therefore not fully understood, and magnetic dilution or bond randomness were not considered in the corresponding paper [24].

In the 6H-Sr phase, the structural disorder suggested by our diffraction data and HAADF-STEM images is essentially associated with the Ni-Sb dumbbell arrangement in a well-crystallized 6H-type triple-perovskite material. As explained in Sec. III A, our results are consistent with either

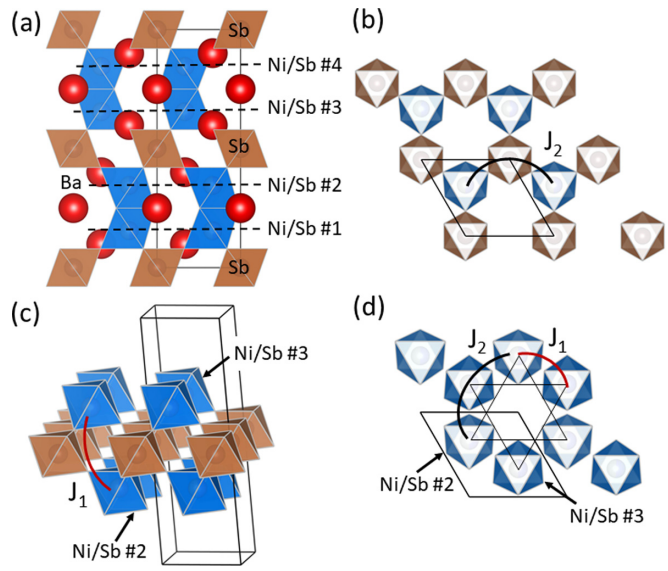

FIG. 16. Nearest neighbor Ni^{2+}-Ni^{2+} interactions in the $P6_3/mmc$ crystal structures of 6HB-HP $Ba_3NiSb_2O_9$ [23] or 6H-Sr $Ba_{2.5}Sr_{0.5}NiSb_2O_9$ (this paper) assuming disorder for the Ni-Sb dumbbell arrangement. SbO_6 and $NiSbO_9$ bi-octahedra (Ni-Sb dumbbells) are colored brown and blue, respectively. (a) View along the b axis. (b) In-plane J_2 interaction in one of the triangular plane of $(Ni/Sb)O_6$ octahedra which are connected by their vertices to single SbO_6 octahedra. (c) Interplane J_1 interaction across a layer of nonmagnetic SbO_6 octahedra. (d) The J_1-J_2 buckled honeycomb lattice formed by two adjacent triangular planes of $(Ni/Sb)O_6$ octahedra. Here, nonmagnetic SbO_6 octahedra are omitted for clarity. Distances and angles for J_1 and J_2 superexchange pathways are given in Supplemental Material [30].

a random orientation of the dumbbells over a crystallite or nanosized chemical correlations for the dumbbell arrangement within the a, b planes. In the latter case, one could deal with a nanosized triangular lattice of Ni^{2+}. In the former case, a random up or down vertical orientation of the dumbbells within a $(NiSbO_9)_\infty$ bilayer would imply that 50% of flipped Ni-Sb dumbbells dilute the triangular lattice of magnetic $S = 1$ cations originally reported in Ref. [12] [shown in Fig. 1(a)] and that the flipped dumbbells insert Ni^{2+} into the adjacent parallel triangular layer of Sb within the same $(NiSbO_9)_\infty$ bilayer. The possible nearest neighbor (NN) superexchange pathways in 6HB-HP and 6H-Sr phases are depicted in Fig. 16. More details on the superexchange angles and distances can be found in the Supplemental Material [30]. Because the main super-superexchange couplings in the c direction occur across the nonmagnetic layers of SbO_6 octahedra, the structure would contain a diluted J_1-J_2 buckled honeycomb lattice consisting of two half-depleted triangular lattices sandwiching a layer of SbO_6 octahedra. The intralayer exchange J_2 in a triangular layer can be viewed as the NNN interaction on the buckled honeycomb, and the interlayer exchange J_1 corresponds to the NN interaction for the buckled honeycomb. It is likely that the situation might be intermediate, interpolating between a diluted triangular lattice and a diluted J_1-J_2 honeycomb model. On a general footing, this points toward the need to consider the introduction of disorder in the physical interpretation of the observed properties.

We first come back to the initial proposal by Cheng *et al.* [12] of an undiluted triangular lattice, which was also considered in Ref. [29]. Studies of the triangular lattice have been much revived after the discovery of a spin-liquid-like state at low temperatures in the rare-earth compound $YbMgGaO_4$ [1–3]. We note that, in the absence of disorder, stabilizing a spin-liquid state requires a large exchange anisotropy [49]. In contrast with that case, working with a 3*d* transition-metal ion such as Ni^{2+} in a weak octahedral crystal field makes such a scenario unrealistic as supported by our electron spin resonance (ESR) data obtained for 6HB-HP $Ba_3NiSb_2O_9$. These ESR data and their analyses are presented in the Supplemental Material [30].

With its even lower coordination, $z = 3$ vs 6 in the triangular case, the honeycomb lattice is more prone to a spin-liquid ground state under isotropic antiferromagnetic interactions if frustration is introduced. This is realized in the J_1-J_2 honeycomb model which has been extensively studied for $S = \frac{1}{2}$ by many theoretical techniques. Although not firmly established, a consensus has emerged that, in a narrow range above $J_2/J_1 \approx 0.23$, a gapless QSL phase could be more favorable than a well-established gapped plaquette valence bond order found to occur for ratios of J_2/J_1 up to ≈ 0.36 [50–54]. While less is known for the $S = 1$ case, it seems that, in the competition between the QSL and the gapped plaquette phase, the latter might be favored, which is contrary to our experimental results [50,53]. Of course, to proceed with a detailed comparison with these numerical results, one should first get some estimate of this ratio through *ab initio* calculations of the exchange parameters, which are beyond the scope of this paper. However, we note that the small difference in the exchange paths for J_1 and J_2 described in the Supplemental Material [30] does not support the idea of a fine tuning of the J_2/J_1 ratio required for that allegated QSL phase.

Disorder could also be an important player in the interpretation of the absence of magnetic order, as was also heavily debated in the context of the $YbMgGaO_4$ triangular compound [4,5,55]. The scenario of a J_1-J_2 disordered honeycomb lattice in 6HB-HP was first discussed at length in Ref. [56] with a proposal for a gapless random singlet phase with orphan spins under the combined effect of frustration and disorder. This proposal seems consistent with published results for 6HB-HP: an upper bound of the disorder parameter $\Delta = \Delta J/J = 0.25$ was estimated from the ^{121}Sb NMR linewidth [24] and could be just enough to stabilize such a phase, as predicted by Uematsu and Kawamura [56] in a revised version from Refs. [57,58] earlier considered in Ref. [24]. Several experimental findings conspire in favor of such a scenario, a linear specific heat was reported [12], peaks of the INS structure factor [29] are smeared out and found at locations different from usual peaks at Γ or K-points in the Brillouin zone for the ordered or plaquette phases.

In a more general context where frustration promotes the formation of local singlets, e.g., for a VBS phase, Kimchi *et al.* [6] have shown how even weak disorder can nucleate $S = \frac{1}{2}$ topological defects and lead to a random spin network with gapless low-energy excitations. Starting, for example, from a honeycomb lattice and the case where the ratio J_2/J_1 does not lead to a QSL or a valence bond scenario in the absence of disorder, we may speculate that disorder could then be the driving force toward a QSL state. This scenario has been involved in the well-studied case of $YbMgGaO_4$ where a power law behavior of the specific heat is found, and the calculated structure factor displays a shallow maximum when second neighbor interactions are included [6]. The similarity with our data shows that structural disorder model might be then the right track to explain the spin-liquid-like behavior in the 6HB-HP and 6*H*-Sr phases.

The cubic crystal structure of 3*C*-Sr $Ba_{1.75}Sr_{1.25}NiSb_2O_9$ is very similar to that of 3*C*-HP $Ba_3NiSb_2O_9$ obtained at 9 GPa [12] so that these compounds should share common features. The Curie-Weiss temperatures θ are indeed comparable, and the higher absolute value of θ in the 3*C*-Sr phase correlates with its smaller cell volume. For both compounds, magnetic specific heats indicated significant magnetic entropy and quadratic behaviors $C_M = \gamma T^2$ at low temperatures, whereas no sign of magnetic transition down to the base temperatures (0.35 or 2 K) was found in the specific heat data. However, our μSR and ^{131}Sb NMR investigation clearly revealed the occurrence of a transition to a magnetic ordered structure below $T_m \approx 11$ K in 3*C*-Sr with a substantial disorder. In the context of what should be a 3D interaction scheme for a FCC lattice, the T^2 behavior of the specific heat instead of a T^3 behavior expected for standard 3D spin waves remains to be explained. In 3*C*-Sr and 3*C*-HP, the $(Ba, Sr)_2BB'O_6$ double perovskite structure is made of two *B* and *B*′ interpenetrating FCC lattices where *B* and *B*′ sites are occupied by Sb and $(Ni_{2/3}Sb_{1/3})$ atoms, respectively. Therefore, both 3*C*-Sr and 3*C*-HP compounds contain a site-diluted FCC sublattice of spin-1 Ni^{2+} cations with 67% site occupancy, which is much higher than the site percolation threshold for a FCC ($p_c^{\text{site}} \approx 20\%$). Thus, either a J_1 or a J_1-J_2 model on the $\frac{1}{3}$-depleted FCC lattice, where J_1 and J_2 are the NN and NNN interactions (displayed in Fig. 2), respectively, are likely to be relevant for explaining the magnetic behaviors. The possible NN and NNN super-superexchange pathways for J_1 and J_2 are described in the Supplemental Material [30]. Here, J_1 interactions occur along Ni–O–O–Ni and 90° Ni-O-Sb-O-Ni pathways with a Ni-Ni distance of 5.71 or 5.77 Å. The former path, which is the shortest, is commonly found to be AFM and dominant over the second one [59,60]. Also, J_2 corresponds to a linear Ni–O–Sb–O–Ni pathway with a Ni–Ni distance of 8.08–8.15 Å. The magnetic behaviors of perovskite oxides that contain octahedral Ni^{2+} and diamagnetic Sb^{5+}, such as $Sr_3NiSb_2O_9$, SrLaNi SbO_6, and $La_3Ni_2SbO_9$, indicate that J_1 and J_2 are AFM and that J_2 is weak due to the completely filled Sb^{5+} 4*d* orbitals [37,61]. For a Heisenberg J_1-J_2 model on a FCC lattice with $J_2/J_1 \sim 0$, theoretical and experimental work for classical spins clearly point to the stabilization of AFM ordering with a stacking of AFM planes which depends on the J_2/J_1 ratio and which can be classified as type I, II, or III [62–64]. Little change is found when one goes from the classical to the quantum case, see, e.g., Ref. [64]. We note that the case $J_2 \approx 0$ leads to a remarkable depression of T_N with respect to larger values of J_2/J_1 [64]. All of this is clearly consistent with our findings of ordering at low temperatures and a sizeable frustration ratio. Moreover, the dilution of the FCC magnetic lattice is clearly in line with the signatures of a substantial disorder of the magnetic structure revealed by the distribution of μSR relaxation rates, the NMR line

broadening above T_m, and the absence of long-lived oscillation of the μ^+ asymmetry and correspondingly the NMR line shape below T_m. Finally, a broad maximum of the relaxation rate occurring only around $0.8\,T_m$ is also seen in the case of triangular chromates [38,39], where a similar observation is clearly established and argued to be a signature of frustration through the persistence of fluctuations well below T_m. Our experimental results are similar to those obtained for 5*d* *B*-site ordered double perovskites containing only one magnetic $S = 1$ cation, namely, La_2LiReO_6 and Ba_2YReO_6 [65], although the spin-orbit coupling might play a major role there in the selection of the ground state. While weak local lattice distortions and possible associated spin Hamiltonian randomness induced by Ba/Sr substitution in 3*C*-Sr might support the idea of a physical difference between the two 3*C* compounds, as reflected in the susceptibility and specific heat data, it is very surprising not to find any hint of a transition in 3*C*-HP $Ba_3NiSb_2O_9$ in the context of the present discussion. A larger low-*T* Curie term from orphan spins could provide a naïve explanation for the lack of signature in the FC-ZFC susceptibility data of Ref. [12]. This certainly calls for a more systematic study of the susceptibility at lower fields and a deeper investigation through μSR, NMR, or low-temperature neutron diffraction.

V. CONCLUDING REMARKS

As in other perovskite oxides, the commonly observed 6*H*-3*C* transformation under physical pressure occurs when the crystal structure of $Ba_3NiSb_2O_9$ is gradually compressed by Sr/Ba chemical substitution. Chemical pressure can provide a simple tool for elaborating perovskite materials with unexplored or modulated electronic properties.

By combining several diffraction techniques, high-resolution *Z*-contrast imaging, and atomic resolution elemental mapping, we have shown that the crystal structures of the 6HB-HP $Ba_3NiSb_2O_9$ and 6*H*-Sr phases feature undistorted triangular lattices of $NiSbO_9$ dumbbells. However, the lack of long-range order in the orientation of the dumbbells and the fact that it is not possible to identify short-range chemical correlations make it difficult to analyze the spin-liquid-like magnetic behavior. The dumbbell disorders certainly lead to complex frustrated magnetic networks and therefore to deviations from clean antiferromagnetic models such as the triangular or the frustrated J_1-J_2 honeycomb. We discussed how this disorder might be the seed for the spin-liquid-like behavior which seems to be relevant in a broader context. The situation regarding the 3*C* phases appears simpler because they can be considered realizations of a diluted FCC lattice of real $S = 1$ spins. Further, our results for the 3*C*-Sr indicate clear differences relative to the pure HP 3*C* system and therefore call for further investigations of these 3*C* phases.

ACKNOWLEDGMENTS

We would like to thank P. Bordet, B. Fåk, A. Ralko, S. Capponi, and B. Gaulin for useful discussions. This work was supported in part by the French Agence Nationale de la Recherche under Grants No. ANR-12-BS04-0021 'SPINLIQ' and No. ANR-18-CE30-0022-04 'LINK'. Funded by the French Contrat Plan État-Région and the European Regional Development Fund of Pays de la Loire, the CIMEN Electron Microscopy Center in Nantes is greatly acknowledged. This work also involved the geochemical analysis facility at Laboratoire de Planétologie et Géosciences (UMR 6112). A.Z. acknowledges the financial support of the Slovenian Research Agency under Program No. P1-0125 and Projects No. BI-US/22-24-065, No. J1-2461, and No. N1-0148. The National High Magnetic Field Laboratory is supported by the National Science Foundation through NSF/DMR-1644779 and the State of Florida.

[1] Y. Li, H. Liao, Z. Zhang, S. Li, F. Jin, L. Ling, L. Zhang, Y. Zou, L. Pi, Z. Yang *et al.*, Gapless quantum spin liquid ground state in the two-dimensional spin-$\frac{1}{2}$ triangular antiferromagnet $YbMgGaO_4$, Sci. Rep. **5**, 16419 (2015).

[2] Y. Li, G. Chen, W. Tong, L. Pi, J. Liu, Z. Yang, X. Wang, and Q. Zhang, Rare-Earth Triangular Lattice Spin Liquid: A Single-Crystal Study of $YbMgGaO_4$, Phys. Rev. Lett. **115**, 167203 (2015).

[3] Y. Li, D. Adroja, P. K. Biswas, P. J. Baker, Q. Zhang, J. Liu, A. A. Tsirlin, P. Gegenwart, and Q. Zhang, Muon Spin Relaxation Evidence for the $U(1)$ Quantum Spin-Liquid Ground State in the Triangular Antiferromagnet $YbMgGaO_4$, Phys. Rev. Lett. **117**, 097201 (2016).

[4] Z. Zhu, P. A. Maksimov, S. R. White, and A. L. Chernyshev, Disorder-Induced Mimicry of a Spin Liquid in $YbMgGaO_4$, Phys. Rev. Lett. **119**, 157201 (2017).

[5] Y. Li, P. Gegenwart, and A. A. Tsirlin, Spin liquids in geometrically perfect triangular antiferromagnets, J. Phys. Condens. Matter **32**, 224004 (2020).

[6] I. Kimchi, A. Nahum, and T. Senthil, Valence Bonds in Random Quantum Magnets: Theory and Application to $YbMgGaO_4$, Phys. Rev. X **8**, 031028 (2018).

[7] Y. Shirata, H. Tanaka, A. Matsuo, and K. Kindo, Experimental Realization of a Spin-$\frac{1}{2}$ Triangular-Lattice Heisenberg Antiferromagnet, Phys. Rev. Lett. **108**, 057205 (2012).

[8] H. D. Zhou, C. Xu, A. M. Hallas, H. J. Silverstein, C. R. Wiebe, I. Umegaki, J. Q. Yan, T. P. Murphy, J.-H. Park, Y. Qiu *et al.*, Successive Phase Transitions and Extended Spin-Excitation Continuum in the $S = \frac{1}{2}$ Triangular-Lattice Antiferromagnet $Ba_3CoSb_2O_9$, Phys. Rev. Lett. **109**, 267206 (2012).

[9] H. D. Zhou, E. S. Choi, G. Li, L. Balicas, C. R. Wiebe, Y. Qiu, J. R. D. Copley, and J. S. Gardner, Spin Liquid State in the $S = \frac{1}{2}$ Triangular Lattice $Ba_3CuSb_2O_9$, Phys. Rev. Lett. **106**, 147204 (2011).

[10] S. Nakatsuji, K. Kuga, K. Kimura, R. Satake, N. Katayama, E. Nishibori, H. Sawa, R. Ishii, M. Hagiwara, F. Bridges *et al.*, Spin-orbital short-range order on a honeycomb-based lattice, Science **336**, 559 (2012).

[11] J. A. Quilliam, F. Bert, E. Kermarrec, C. Payen, C. Guillot-Deudon, P. Bonville, C. Baines, H. Luetkens, and P. Mendels, Singlet Ground State of the Quantum Antiferromagnet $Ba_3CuSb_2O_9$, Phys. Rev. Lett. **109**, 117203 (2012).

[12] J. G. Cheng, G. Li, L. Balicas, J. S. Zhou, J. B. Goodenough, C. Xu, and H. D. Zhou, High-Pressure Sequence of $Ba_3NiSb_2O_9$

Structural Phases: New $S = 1$ Quantum Spin Liquids Based on Ni^{2+}, Phys. Rev. Lett. **107**, 197204 (2011).

[13] T. Susuki, N. Kurita, T. Tanaka, H. Nojiri, A. Matsuo, K. Kindo, and H. Tanaka, Magnetization Process and Collective Excitations in the $S = \frac{1}{2}$ Triangular-Lattice Heisenberg Antiferromagnet $Ba_3CoSb_2O_9$, Phys. Rev. Lett. **110**, 267201 (2013).

[14] J. Ma, Y. Kamiya, T. Hong, H. B. Cao, G. Ehlers, W. Tian, C. D. Batista, Z. L. Dun, H. D. Zhou, and M. Matsuda, Static and Dynamical Properties of the Spin-$\frac{1}{2}$ Equilateral Triangular-Lattice Antiferromagnet $Ba_3CoSb_2O_9$, Phys. Rev. Lett. **116**, 087201 (2016).

[15] S. Ito, N. Kurita, H. Tanaka, S. Ohira-Kawamura, K. Nakajima, S. Itoh, K. Kuwahara, and K. Kakurai, Structure of the magnetic excitations in the spin-$\frac{1}{2}$ triangular-lattice Heisenberg antiferromagnet $Ba_3CoSb_2O_9$, Nat. Commun. **8**, 235 (2017).

[16] Y. Han, M. Hagiwara, T. Nakano, Y. Nozue, K. Kimura, M. Halim, and S. Nakatsuji, Observation of the orbital quantum dynamics in the spin-$\frac{1}{2}$ hexagonal antiferromagnet $Ba_3CuSb_2O_9$, Phys. Rev. B **92**, 180410(R) (2015).

[17] A. Smerald and F. Mila, Disorder-Driven Spin-Orbital Liquid Behavior in the $Ba_3XSb_2O_9$ Materials, Phys. Rev. Lett. **115**, 147202 (2015).

[18] Y. Wakabayashi, D. Nakajima, Y. Ishiguro, K. Kimura, T. Kimura, S. Tsutsui, A. Q. R. Baron, K. Hayashi, N. Happo, S. Hosokawa *et al.*, Chemical and orbital fluctuations in $Ba_3CuSb_2O_9$, Phys. Rev. B **93**, 245117 (2016).

[19] M. Altmeyer, F. Mila, A. Smerald, and R. Valentí, Cu-Sb dumbbell arrangement in the spin-orbital liquid candidate $Ba_3CuSb_2O_9$, Phys. Rev. B **96**, 115116 (2017).

[20] H. Man, M. Halim, H. Sawa, M. Hagiwara, Y. Wakabayashi, and S. Nakatsuji, Spin-orbital entangled liquid state in the copper oxide $Ba_3CuSb_2O_9$, J. Phys. Condens. Matter **30**, 443002 (2018).

[21] P. D. Battle, C. W. Jones, P. Lightfoot, and R. Strange, High-pressure phase transitions in the 6*H* perovskites $Ba_3MSb_2O_9$ (M = Mg, Ni, Zn), J. Solid State Chem. **85**, 144 (1990).

[22] A. J. Jacobson and A. J. Calvert, A powder neutron diffraction study of cation ordering in 6*H* $Ba_3Sb_2NiO_9$, J. Inorg. Nucl. Chem. **40**, 447 (1978).

[23] C. Darie, C. Lepoittevin, H. Klein, S. Kodjikian, P. Bordet, C. V. Colin, O. I. Lebedev, C. Deudon, and C. Payen, A new high pressure form of $Ba_3NiSb_2O_9$, J. Solid State Chem. **237**, 166 (2016).

[24] J. A. Quilliam, F. Bert, A. Manseau, C. Darie, C. Guillot-Deudon, C. Payen, C. Baines, A. Amato, and P. Mendels, Gapless quantum spin liquid ground state in the spin-1 antiferromagnet 6HB-$Ba_3NiSb_2O_9$, Phys. Rev. B **93**, 214432 (2016).

[25] R. D. Shannon, Revised effective ionic radii and systematic studies of interatomic distances in halides and chalcogenides, Acta Crystallogr. A **32**, 5 (1976).

[26] Q. Zhou, T.-Y. Tan, B. J. Kennedy, and J. R. Hester, Crystal structures and phase transitions in Sr doped Ba_2InTaO_6 perovskites, J. Solid State Chem. **206**, 122 (2013).

[27] J. Li, P. Jiang, W. Gao, R. Cong, and T. Yang, Chemical substitution-induced and competitive formation of 6*H* and 3*C* perovskite structures in $Ba_{3-x}Sr_xZnSb_2O_9$: The coexistence of two perovskites in $0.3 \leqslant x \leqslant 1.0$, Inorg. Chem. **56**, 14335 (2017).

[28] P. Kayser, S. Injac, B. J. Kennedy, T. Vogt, M. Avdeev, H. E. Maynard-Casely, and Z. Zhang, Structural and magnetic properties of the osmium double perovskites $Ba_{2-x}Sr_xYOsO_6$, Inorg. Chem. **56**, 6565 (2017).

[29] B. Fåk, S. Bieri, E. Canévet, L. Messio, C. Payen, M. Viaud, C. Guillot-Deudon, C. Darie, J. Ollivier, and P. Mendels, Evidence for a spinon fermi surface in the triangular $S = 1$ quantum spin liquid $Ba_3NiSb_2O_9$, Phys. Rev. B **95**, 060402(R) (2017).

[30] See Supplemental Material at http://link.aps.org/supplemental/10.1103/PhysRevMaterials.6.124408 for details on the synthesis and characterization, superexchange interactions, and ESR study of HP 6HB $Ba_3NiSb_2O_9$, which includes Refs. [12,23,31,66–79].

[31] V. Petricek, M. Dusek, and L. Palatinus, Crystallographic computing system JANA2006: General features, Z. Für Krist. **229**, 345 (2014).

[32] K. Momma and F. Izumi, VESTA 3 for three-dimensional visualization of crystal, volumetric and morphology data, J. Appl. Crystallogr. **44**, 1272 (2011).

[33] L. Palatinus, PETS—program for analysis of electron diffraction data, Institute of Physics of the CAS, Praha, Czechia, 2011.

[34] M. T. Anderson, K. B. Greenwood, G. A. Taylor, and K. R. Poeppelmeier, B-cation arrangements in double perovskites, Prog. Solid State Chem. **22**, 197 (1993).

[35] G. King and P. M. Woodward, Cation ordering in perovskites, J. Mater. Chem. **20**, 5785 (2010).

[36] M. James, J. P. Attfield, and J. Rodriguez-Carvajal, Synthesis, crystal structure and magnetism of $Sr_3Sb_2NiO_9$—a ferrimagnetic perovskite, J. Phys. Chem. Solids **56**, 1331 (1995).

[37] P. D. Battle, C.-M. Chin, S. I. Evers, and M. Westwood, Structure and magnetism of $Sr_3NiSb_2O_9$, J. Solid State Chem. **227**, 1 (2015).

[38] A. Olariu, P. Mendels, F. Bert, B. G. Ueland, P. Schiffer, R. F. Berger, and R. J. Cava, Unconventional Dynamics in Triangular Heisenberg Antiferromagnet $NaCrO_2$, Phys. Rev. Lett. **97**, 167203 (2006).

[39] K. Somesh, Y. Furukawa, G. Simutis, F. Bert, M. Prinz-Zwick, N. Büttgen, A. Zorko, A. A. Tsirlin, P. Mendels, and R. Nath, Universal fluctuating regime in triangular chromate antiferromagnets, Phys. Rev. B **104**, 104422 (2021).

[40] R. S. Hayano, Y. J. Uemura, J. Imazato, N. Nishida, T. Yamazaki, and R. Kubo, Zero-and low-field spin relaxation studied by positive muons, Phys. Rev. B **20**, 850 (1979).

[41] A. Keren, Generalization of the Abragam relaxation function to a longitudinal field, Phys. Rev. B **50**, 10039 (1994).

[42] Y. J. Uemura, A. Keren, K. Kojima, L. P. Le, G. M. Luke, W. D. Wu, Y. Ajiro, T. Asano, Y. Kuriyama, M. Mekata *et al.*, Spin Fluctuations in Frustrated Kagomé Lattice System $SrCr_8Ga_4O_{19}$ Studied by Muon Spin Relaxation, Phys. Rev. Lett. **73**, 3306 (1994).

[43] D. Bono, P. Mendels, G. Collin, N. Blanchard, F. Bert, A. Amato, C. Baines, and A. D. Hillier, μSR Study of the Quantum Dynamics in the Frustrated $S = \frac{3}{2}$ Kagomé Bilayers, Phys. Rev. Lett. **93**, 187201 (2004).

[44] P. Khuntia, F. Bert, P. Mendels, B. Koteswararao, A. V. Mahajan, M. Baenitz, F. C. Chou, C. Baines, A. Amato, and Y. Furukawa, Spin Liquid State in the 3*d* Frustrated Antiferromagnet $PbCuTe_2O_6$: NMR and Muon Spin Relaxation Studies, Phys. Rev. Lett. **116**, 107203 (2016).

[45] V. M. Goldschmidt, Die Gesetze der Krystallochemie, Naturwissenschaften **14**, 477 (1926).

[46] P. M. Woodward, Octahedral tilting in perovskites. II. Structure stabilizing forces, Acta Cryst. B **53**, 44 (1997).

[47] R. Mani, P. Selvamani, J. E. Joy, J. Gopalakrishnan, and T. K. Mandal, Study of $Ba_3M^{II}M^{IV}WO_9$ (M^{II} = Ca, Zn; M^{IV} = Ti, Zr) perovskite oxides: competition between 3*C* and 6*H* perovskite structures, Inorg. Chem. **46**, 6661 (2007).

[48] J. B. Goodenough and J. A. kafalas, Exploring the $A^+B^{5+}O_3$ compounds, J. Solid State Chem. **6**, 493 (1973).

[49] Z. Zhu, P. A. Maksimov, S. R. White, and A. L. Chernyshev, Topography of Spin Liquids on a Triangular Lattice, Phys. Rev. Lett. **120**, 207203 (2018).

[50] S.-S. Gong, W. Zhu, and D. N. Sheng, Quantum phase diagram of the spin-1 J_1-J_2 Heisenberg model on the honeycomb lattice, Phys. Rev. B **92**, 195110 (2015).

[51] F. Ferrari, S. Bieri, and F. Becca, Competition between spin liquids and valence-bond order in the frustrated spin $-\frac{1}{2}$ Heisenberg model on the honeycomb lattice, Phys. Rev. B **96**, 104401 (2017).

[52] A. F. Albuquerque, D. Schwandt, B. Hetényi, S. Capponi, M. Mambrini, and A. M. Läuchli, Phase diagram of a frustrated quantum antiferromagnet on the honeycomb lattice: Magnetic order versus valence-bond crystal formation, Phys. Rev. B **84**, 024406 (2011).

[53] J. Merino and A. Ralko, Role of quantum fluctuations on spin liquids and ordered phases in the Heisenberg model on the honeycomb lattice, Phys. Rev. B **97**, 205112 (2018).

[54] The proposal of G. Chen *et al.*, [G. Chen, M. Hermele, and L. Radzihovsky, Phys. Rev. Lett. **109**, 016402 (2012)] to consider being close to a quantum critical point requires a substantial single-ion anisotropy and leads to a gapped state; both are not the case here.

[55] H.-Q. Wu, S.-S. Gong, and D. N. Sheng, Randomness-induced spin-liquid-like phase in the spin $-\frac{1}{2}$ J_1-J_2 triangular Heisenberg model, Phys. Rev. B **99**, 085141 (2019).

[56] K. Uematsu and H. Kawamura, Randomness-induced quantum spin liquid behavior in the $S = \frac{1}{2}$ random J_1-J_2 Heisenberg antiferromagnet on the honeycomb lattice, J. Phys. Soc. Jpn. **86**, 044704 (2017).

[57] K. Watanabe, H. Kawamura, H. Nakano, and T. Sakai, Quantum spin-liquid behavior in the spin-$\frac{1}{2}$ random Heisenberg antiferromagnet on the triangular lattice, J. Phys. Soc. Jpn. **83**, 034714 (2014).

[58] T. Shimokawa, K. Watanabe, and H. Kawamura, Static and dynamical spin correlations of the $S = \frac{1}{2}$ random-bond antiferromagnetic Heisenberg model on the triangular and kagome lattices, Phys. Rev. B **92**, 134407 (2015).

[59] Z. Lu, L. Ge, G. Wang, M. Russina, G. Günther, C. R. dela Cruz, R. Sinclair, H. D. Zhou, and J. Ma, Lattice distortion effects on the frustrated spin-1 triangular-antiferromagnet $A_3NiNb_2O_9$ (A = Ba, Sr, and Ca), Phys. Rev. B **98**, 094412 (2018).

[60] R. Rawl, M. Lee, E. S. Choi, G. Li, K. W. Chen, R. Baumbach, C. R. dela Cruz, J. Ma, and H. D. Zhou, Magnetic properties of the triangular lattice magnets $A_4B'B_2O_{12}$ (A = Ba, Sr, La; B' = Co, Ni, Mn; B = W, Re), Phys. Rev. B **95**, 174438 (2017).

[61] C.-M. Chin, P. D. Battle, A. L. Goodwin, and A. Wildes, Short-range cation and spin ordering in the relaxor ferromagnet $La_3Ni_2SbO_9$ studied by polarized-neutron scattering and Monte-Carlo methods, J. Solid State Chem. **278**, 120920 (2019).

[62] M. S. Seehra and T. M. Giebultowicz, Magnetic structures of fcc systems with nearest-neighbor and next-nearest-neighbor exchange interactions, Phys. Rev. B **38**, 11898 (1988).

[63] J. S. Smart, *Effective Field Theories of Magnetism* (Saunders, Philadelphia, London, 1966).

[64] N.-N. Sun and H.-Y. Wang, The J_1-J_2 model on the face-centered-cubic lattices, J. Magn. Magn. Mater. **454**, 176 (2018).

[65] T. Aharen, J. E. Greedan, C. A. Bridges, A. A. Aczel, J. Rodriguez, G. MacDougall, G. M. Luke, V. K. Michaelis, S. Kroeker, C. R. Wiebe *et al.*, Structure and magnetic properties of the $S = 1$ geometrically frustrated double perovskites La_2LiReO_6 and Ba_2YReO_6, Phys. Rev. B **81**, 064436 (2010).

[66] G. E. Pake, *Paramagnetic Resonance: An Introductory Monograph* (WA Benjamin, New York, 1962).

[67] A. Zorko, Determination of magnetic anisotropy by EPR, in *Topics from EPR Research*, edited by A. M. Maghraby (IntechOpen, London, 2019).

[68] M. S. Seehra and T. G. Castner, The paramagnetic line width in $Cu(HCOO)_2 \cdot 4H_2O$, Phys. Kondens. Materie **7**, 185 (1968).

[69] D. L. Huber and M. S. Seehra, Contribution of the spin-phonon interaction to the paramagnetic resonance linewidth of $CrBr_3$, J. Phys. Chem. Solids **36**, 723 (1975).

[70] M. S. Seehra, M. M. Ibrahim, V. S. Babu, and G. Srinivasan, The linear temperature dependence of the paramagnetic resonance linewidth in the manganate perovskites $La_{0.67}Sr_{0.33}MnO_3$ and $La_{0.62}Bi_{0.05}Ca_{0.33}MnO_3$, J. Phys.: Condens. Matter **8**, 11283 (1996).

[71] J. Deisenhofer, S. Schaile, J. Teyssier, Z. Wang, M. Hemmida, H.-A. Krug von Nidda, R. M. Eremina, M. V. Eremin, R. Viennois, E. Giannini *et al.*, Electron spin resonance and exchange paths in the orthorhombic dimer system Sr_2VO_4, Phys. Rev. B **86**, 214417 (2012).

[72] A. Zorko, D. Arčon, H. van Tol, L. C. Brunel, and H. Kageyama, X-band ESR determination of Dzyaloshinsky-Moriya interaction in the two-dimensional $SrCu_2(BO_3)_2$ system, Phys. Rev. B **69**, 174420 (2004).

[73] A. Zorko, F. Bert, A. Ozarowski, J. van Tol, D. Boldrin, A. S. Wills, and P. Mendels, Dzyaloshinsky-Moriya interaction in vesignieite: A route to freezing in a quantum kagome antiferromagnet, Phys. Rev. B **88**, 144419 (2013).

[74] A. Zorko, D. Arčon, A. Lappas, J. Giapintzakis, C. Saylor, and L. C. Brunel, Effect of vacancy doping on the Haldane spin-liquid state in $PbNi_{2-x}Mg_xV_2O_8$, Phys. Rev. B **65**, 144449 (2002).

[75] M. Heinrich, H.-A. Krug Von Nidda, A. Loidl, N. Rogado, and R. J. Cava, Potential Signature of a Kosterlitz-Thouless Transition in $BaNi_2V_2O_8$, Phys. Rev. Lett. **91**, 137601 (2003).

[76] Y. Maeda, K. Sakai, and M. Oshikawa, Exact Analysis of ESR Shift in the Spin-$\frac{1}{2}$ Heisenberg Antiferromagnetic Chain, Phys. Rev. Lett. **95**, 037602 (2005).

[77] R. Kubo and K. Tomita, A general theory of magnetic resonance absorption, J. Phys. Soc. Jpn. **9**, 888 (1954).

[78] A. Zorko, S. Nellutla, J. van Tol, L. C. Brunel, F. Bert, F. Duc, J.-C. Trombe, M. A. de Vries, A. Harrison, and P. Mendels, Dzyaloshinsky-Moriya Anisotropy in the Spin-$\frac{1}{2}$ Kagome Compound $ZnCu_3(OH)_6Cl_2$, Phys. Rev. Lett. **101**, 026405 (2008).

[79] T. Moriya, Anisotropic superexchange interaction and weak ferromagnetism, Phys. Rev. **120**, 91 (1960).